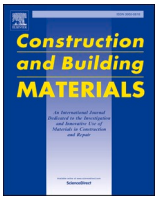
Construction and Building Materials 408 (2023) 133686



Contents lists available at ScienceDirect

Construction and Building Materials

journal homepage: www.elsevier.com/locate/conbuildmat





Simultaneous desalination and consolidation treatment through the application of electrokinetic techniques

J. Feijoo [a,*], L.S. Gomez-Villalba [b], R. Fort [b,*], M.E. Rabanal [c]

[a] Defense University Center at Spanish Naval Academy, University of Vigo, Plaza de España 2, 36920 Marín, Pontevedra, Spain
[b] Institute of Geosciences IGEO (CSIC, UCM), c/Doctor Severo Ochoa, 7, 28040 Madrid, Spain
[c] Carlos III University of Madrid and IAAB, Department of Materials Science and Engineering and Chemical Engineering, Avda. de la Universidad 30, 28911 Leganes, Madrid, Spain

ARTICLE INFO

Keywords:
Electrokinetic technique
Electro precipitation
Desalination
Consolidation
Soluble salts
Limestone
Dolomite

ABSTRACT

The vast majority of building materials that are heavily affected by salts require desalination and subsequent consolidation treatments. This double intervention entails a risk associated with the loss of material due to continuous contact with the affected surface. This study evaluates the effectiveness of an electrokinetic process of simultaneous desalination-consolidation of two types of stones (dolostone and limestone). The results show that it is possible to reduce the salts up to percentages of 100% and at the same time to fill the pores and fractures with insoluble compounds compatible with the materials to be treated, such as calcium-magnesium carbonates.

1. Introduction

Over the years, the exposure of porous building materials used both in modern buildings and architectural heritage, to aggressive environmental conditions, both natural (i.e., water, soluble salts, biocolonization) and anthropogenic (air pollution), can induce some degradation processes. Among the degradation processes that affect porous building materials, it is worth mentioning the damages associated with the internal pressures that soluble salts generate when crystalizing inside the material's pores [1]. As the soluble salts precipitate inside the pores, the growth of salt crystals can generate pressures [2–4], which can exceed the tensile strength of the materials causing damage or even their breakage. This damage is favored by the existence of repeated dissolution/deliquescence and crystallization cycles [5–7], as a consequence of their contact with water (either in liquid or vapor form respectively). As a result, the loss of cohesion of the grains at the surface or the presence of superficial detachments with different thicknesses can take place [8]. Consequently, the process can endanger the historic value of the property, since it is a non-renewable resource with unique and irreplaceable value, or even endanger its perpetuation, due to the development in the worst scenarios of structural problems.

These processes, by which all building constructions are affected, are expected to worsen in the near future due to climate change. The main reason is the impact of climate change on the damage caused by salt weathering, due to the influence exerted by the environmental parameters on the salt transition phases [9,10]. For this reason, it is crucial to develop new techniques and treatments that allow the safeguarding of the integrity of building constructions.

The different alteration agents mentioned above (water, biocolonization and air pollution) participate in some way in the damage caused by soluble salts, either as a source of salts or as a means of their transport. Numerous studies that relate the source of soluble salts inside the porous building materials with: 1) a leaching process from building materials. In this sense, sulfates are usually attributed to this source due to the leaching of plaster-based coatings, Portland cement mortars [11,12] and other kinds of mortars (for example those rich in magnesium, which are sources of magnesium sulfate [13]); 2) atmospheric deposition. It is documented that air pollution, caused for example by emissions from fossil fuels burned by vehicles [14,15] or the presence of mining and cement plants [16,17], may be the source of sulfates. The seawater spray is the main source of chlorides [18], being able to reach distances even farther than 20 km inland [19]; 3) remnants of old treatments such as: the use of oxalic acid on the marble to give it a yellowish appearance, which causes calcium oxalate crystals [20], or the application of certain consolidation treatments, such as the use of potassium aluminate [21] or either sodium and potassium silicates. These

* Corresponding authors.
E-mail addresses: jfeijoo@cud.uvigo.es (J. Feijoo), luzgomez@geo.ucm.es (L.S. Gomez-Villalba), rafael.fort@csic.es (R. Fort).

https://doi.org/10.1016/j.conbuildmat.2023.133686
Received 27 July 2023; Received in revised form 17 September 2023; Accepted 4 October 2023
Available online 11 October 2023
0950-0618/© 2023 The Authors. Published by Elsevier Ltd. This is an open access article under the CC BY-NC-ND license (http://creativecommons.org/licenses/by-nc-nd/4.0/).

inorganic consolidants can evolve after hydrolyzing processes to form potassium or sodium sulfate by reacting potassium or sodium hydroxide with the atmospheric SO_3 [22]; 4) a biological source, related with the secretion of acids from biological organisms. For example, this is the case with calcium sulfate, which can be formed by the secretion of inorganic sulfuric acid from fungi and its reaction with calcite minerals [23], and calcium oxalate crystals by the interaction between organic acids and carbonate minerals [24]. Also, bone debris and animal droppings, which once dissolved in water, are a source of phosphate salts of magnesium and calcium, as well as nitrates and chlorides [25]. 5) groundwater rising through foundations by capillary suction. In rural areas, the main salts are sulfates and nitrates, since both anions are part of fertilizer composition [26], while in urban areas the presence of chlorides, nitrates, and sulfates stands out [1,26,27].

Up to now, no technically feasible solutions exist to remove or stop the damage caused by salt crystallization, unless removing either the salt source or the moisture source. This is due to, despite the diverse origin that salts may have, their entry into the porous material occurs, in all cases, through their previous dissolution in water. For this reason, the main strategies applied by professionals are focused on: 1) controlling the environmental conditions (temperature and relative humidity) in order to hinder the existence of cyclic dissolution-crystallization processes of salts [28]. For this purpose, is necessary to maintain the conditions either below or above the crystallization point of the salts present in the building. 2) reducing, as far as possible, the ion content in the material by applying some desalination techniques: immersion baths [29], application of poultices or sacrificial mortars [30–33], use of crystallization modifiers [34–36], among others. Recent studies show that the application of electrokinetic techniques allows the reduction of the anion content, both at laboratory scale [37,38] and on-site [39,40], in percentages close to 100 %. 3) to hinder the entrance of these aggressive alteration agents to the interior of the material by reducing the accessible porosity. In this sense, the application of consolidants and water-repellent stands out.

On numerous occasions the material to be treated is so altered that it is only possible to carry out: 1) The replacement, in the worst case, of the weathered stones by new ones, which in some cases could affect to the authenticity and value of the monument. 2) To return the cohesion between the mineral grains of the material by the application of some consolidation treatments, prior to applying any other treatment (i.e., apply it as a pre-consolidation treatment). However, the detachment of part of the altered material, due to the direct contact between this zone and the pre-consolidation treatment applied can affect to the value of the monument. This is because the material's surface is usually the one that has a high historical value due to the carved areas (such as capitals and columns) and the possible existence of polychromies. Furthermore, as reported in [41,42], the application of a pre-consolidation treatment reduces the effectiveness of subsequent desalination treatments applied on the same area, or at least those based on the use of immersion baths and poultices. 3) To treat the affected surface from adjacent areas that show a lesser degree of deterioration or whose value is less. In this sense, electrokinetic techniques in previous studies have shown that it is possible to carry out this type of intervention [43,44].

In addition to this, and despite the evolution in recent years that is taking place in the consolidation field with the synthesis of new nanomaterials, it should be noted that the results obtained at a laboratory are far from those obtained on site. This is due to the fact that the vast majority of the studies are carried out under ideal laboratory conditions for their behavior, such as: low or no salt and moisture content. However, when on site, the vast majority of buildings always have a certain degree of humidity and salt. Both factors have a direct influence on the dry matter of the product that remains in the material, either by reducing the available pore volume for its absorption [45] and also increasing the hydrolysis rate of the sol–gel reaction (this fact increases the viscosity of the consolidant reducing its penetration depth [46–48]).

Recently, a new consolidation procedure based on electrochemical principles has been developed [49–52]. This technique, respectful to the environment and with low toxicity for the people who apply it, allows the precipitation of inorganic compounds on demand inside the pores of a material. Like the rest of the electrokinetic treatments, this technique is favored by the presence of moisture since it will facilitate the transport of the current. Likewise, it is expected that the technique will be improved by the presence of a previous ionic content inside the material (a fact that has not yet been verified).

Despite the technological advances and new techniques developed in recent years, at this moment, no procedure gets the consolidation of a deteriorated material while simultaneously allowing the removal of the salts causing the damage. This concern is mainly due to the risk that the consolidating treatment polymerizes close to the surface and does not let out the salts that have to be mobilized towards the surface, producing an accumulation of sub-florescences in the most superficial layers, which increases the damage caused by internal crystallization of soluble salts in the material [53,54]. This fact might be more counterproductive as it accelerates the material's alteration process.

This study aims to dive into the existing knowledge on electrokinetic techniques and assesses their suitability as a simultaneously desalination and consolidation techniques, using types of stones (limestone and dolomite) highly contaminated by salts (chloride, sulfate, and nitrate)for that purpose, which will be consolidated by the electro-precipitation of a magnesium, calcium or calcium-magnesium carbonate.

2. Material and methods

2.1. Stones used

For this study, two different ornamental rocks widely used in the architectural heritage of Madrid (Spain) were selected: Redueña (upper cretaceous dolostone extracted from abandoned quarries located at Redueña, municipality of Madrid) and Blue Bateig (biocalcarenite stone extracted from quarries located between Elda and Novelda, both municipalities of Alicante). Both stones, as stated in [55,56] and also those that can be seen directly in the monuments built with these stones, are highly sensible to the damage caused by the action of soluble salts.

In this study, a total of eighteen cylindrical specimens (9 of Redueña and 9 of Blue Bateig), of 54 mm in diameter and 30 mm length, were used.

All specimens, except one per kind of stone, were contaminated with a saline solution composed in weight of NaCl 10 %, KNO_3 8 %, and $CaSO_4$ 0.2 %. This solution contains a mixture of the most frequent anions and cations found in monuments according to [21,57], which also have different ionic mobility under the action of the electric field [58]: Cl^- 7.19, NO_3^- 7.40, SO_4^{2-} 8.29, Na^+ 5.19, Ca^{2+} 6.17 and, K^+ 7.62 (all of them in 10^{-8} $m^2/V{\cdot}s$). This different mobility has an influence on the desalination process, since the less soluble and less mobile salts, such as sulfates, followed by nitrates and finally chlorides, are the most difficult to extract from the interior of a porous material. To facilitate the salt contamination, eight specimens per stone were subjected to periodic cycles consisting of 3 days of capillary absorption followed by 2 days of drying at room temperature, a similar procedure to that used in [37,38]. Every cycle, it was used to change the contact surface between the specimen and the saline solution, in order to get as far as possible a homogeneous distribution of the salts. A total of 5 cycles were made.

Before carrying out the salt contamination cycles, some properties per stone were characterized.

Mineralogy was done on the block surface, without crushing, by X-ray diffraction using a high-sensitivity Philips XPERT-PRO diffractometer, an XCelerator with RTMS detector operating continuously in 2θ ranges from 4° to 80° with a step size of 0.0334° and step time 50.165 s counts per step, and Cu-K Alpha radiation. The mineralogical phases were identified using the Panalytical X'Pert High Score database, endorsed by the ICDD (International Center for Diffraction Data), the Joint Committee on Powder Diffraction Standards (JCPDS) and the

American Mineralogist Crystal Structure database (AMCSD).

Petrography was studied by Transmitted and Reflected Polarized Light Optical Microscopy (PLOM) in thin sections, to identify the texture and mineral properties of samples before and after treatments. The Olympus *trans*-Ref BX 53 polarized light microscope equipped with bright field (FBF) and dark (FDF) filters allowed us to obtain transmitted and reflected light images respectively. The interpretation was done by using Olympus Stream Essential software and Micrograph TM Gatan digital software.

Textural properties and chemical composition were determined via environmental scanning electron microscopy (ESEM) and energy dispersive X-ray spectroscopy (EDX) using a FEI Inspect ESEM, equipped with an EDS probe operating in low vacuum mode. The spatial distribution of elements was performed to obtain EDX elemental mapping images and textures for each sample.

Physical properties are related to the pore structure of both stones. In this case, some properties such as: water accessible porosity, bulk density, and capillary water absorption coefficient were determined following the procedure established in different European standards ([59,60] respectively), and using 9 cylindrical specimens per stone. Also the capillary porosity was determined using the expression collected in [61], which was used in other studies [50,51]. Pore size distribution and mercury accessible porosity (MAP) were assessed by mercury intrusion porosimetry (MIP), using an Autpore IV9500 porosimeter of Micromeritics. This porosimeter allows the characterization of pores with an access diameter between 360 μm and 3.8 nm. The measurements were conducted, and duplicated, on stone prisms of 10 mm in diameter and 20 mm high.

Regarding mechanical properties, ultrasonic pulse velocity (UPV) was measured for each of the nine cylindrical specimens per stone, in the same direction of the current flow (i.e., between the surfaces in contact with the cells C3 of the assembly used in this study, see Fig. 1). A total of 7 measurements per specimen were taken on dry samples using a PUNDIT CNS Electronics (precision: ± 0.1 μs) and transducers of 1 MHz of frequency and 11.82 mm in diameter. After discarding the highest and lowest value, the average of the other five values was taken as the accepted value. Considering the correlation between UPV and uniaxial compressive strength (UCS) in porous building materials [62–64], this parameter has been determined indirectly using the model proposed by [65] for limestone: UCS (MPa) = 0.0159· UPV(m/s) – 27.172.

Color characterization was made for all the nine specimens per stone in both cylindrical surfaces. For this purpose, 10 random measurements were made per surface (i.e., 20 measurements per specimen), using a Minolta CM-700d spectrophotometer, and the colors were expressed in the CIE Lab color space. The measurements were taken, including the specular component, with a spot diameter of 8 mm, using a D65 illuminant, and an observed angle of 10°.

After carrying out the salt contamination process, and once the samples were dried to constant weight, the textural properties by ESEM-EDX, petrographic analyses by PLOM, UPV, and color characterization were assessed again using the same equipment stated before. Furthermore, in two specimens per stone, the anion content was quantified by high resolution chromatography (IC). For that purpose, each specimen was segmented into two pieces (from each surface to the middle of the stone), by hammer and chisel. Each fragment was milled and homogenized. After that, 0.15 g of powder were taken and were immersed in 15 mL of ultrapure water. After being stirred by ultrasound waves for 45 min and filtered through 0.45 μm opening mesh sieve, the anion content was measured by IC using a Metrohm 761 Compact IC ion chromatograph.

2.2. Electrokinetic desalination setup

Fig. 1 shows the assembly used for this study, which comprises two electrode compartments (anodic and cathodic), each one placed on each side of the porous material. Each electrode compartment consists of three cells (C1-C3).

Cells C1 are those furthest from the material to be treated. In these cells, either the electrodes (in this study titanium mesh electrodes coated with mixed metal oxides were used) or the solutions that supplying the precursors necessary to the consolidation, are hosted. During the treatment, it is expected that the initial pH of each solution will be modified due to the electrolysis of water that takes place on each electrode's surface (Eqs. (1) and (2)). In this sense, acidification, at the anode, and alkalinization, at the cathode, occurs.

$$\text{Anode: } H_2O \rightarrow 2H^+ + 1/2O_{2(g)} + 2e^- \quad (1)$$

$$\text{Cathode } 2H_2O + 2e^- \rightarrow 2OH^- + H_{2(g)} \quad (2)$$

In order to preventextreme pH values from reaching the surface of the stony material, a cell C2 filled with a material with pH buffering ability is located immediately after the cell C1. At the anode, the material used was a poultice made of magnesium carbonate:kaolin:ultrapure water in a 2:1:6 proportion by weight (named as P-A1), similar

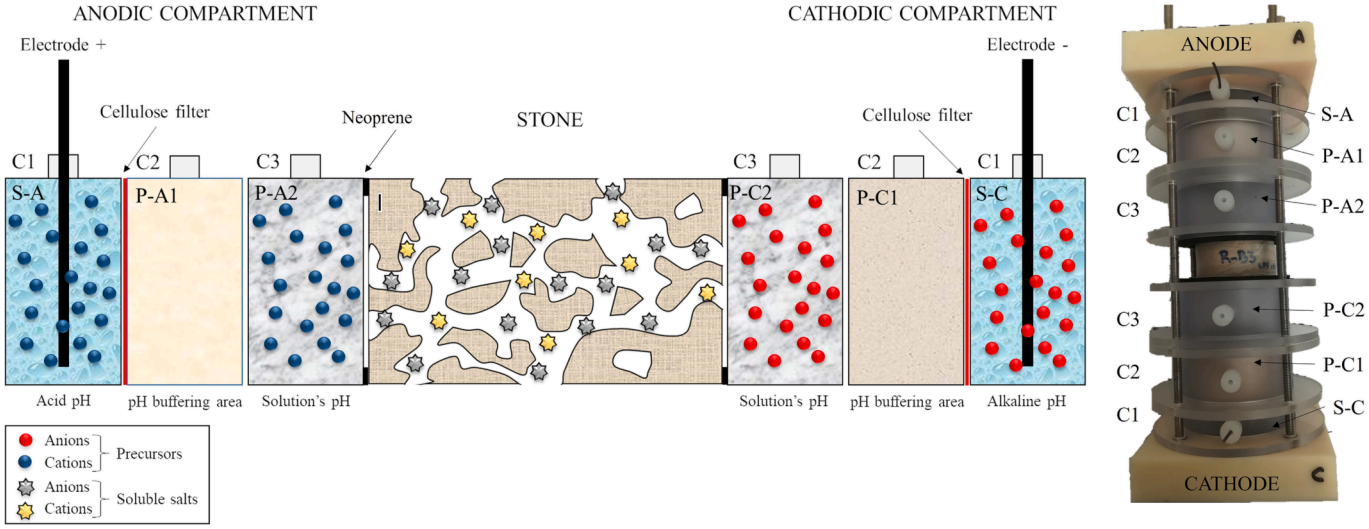


Fig. 1. Schematic diagram and photograph of the assembly used to treat the porous material affected by salts. The distribution of the cells which hosted the different elements used (i.e., poultices, solutions, electrodes), both for desalination and consolidation, can be noted. Also, the initial distribution of the anions and cations, both those used as precursors (circles) and those that are the soluble salts (stars), is shown.

poultice to that used in [49,50]. The decomposition of magnesium carbonate at acidic pH values allows the buffering of the pH (Eqs. (3) and (4)), preventing the acidic environment from reaching the surface of the material to be treated, as demonstrated in [50]. At the same time, the decomposition of this compound increases the concentration of Mg^{2+} free ions, which can be supplied to the stone (cation used as a precursor in this study).

$$MgCO_3 + H^+ \rightarrow Mg^{2+} + HCO_3^- \quad (3)$$

$$HCO_3^- + H^+ \rightarrow CO_{2(g)} + H_2O \quad (4)$$

At the cathode, the material used was a poultice made of kaolin:ultrapure water in a proportion 1.5:1 by weight (named as P-C1). The high ion exchange capacity of kaolin hinder the migration of OH^- ions towards the material's surface, as demonstrated in [66,67].

At both compartments, cellulose filters were used between the cells C1 and C2 in order to prevent the spreading of the poultice into the solution.

Finally, in direct contact both with the poultice hosted in cells C2 and with the surface of the material to be treated are located the cells C3. These two cells hosted, in both compartments, a poultice made of cellulose:solution that supply the precursors (i.e. the ions necessary to carrying out the precipitation of an insoluble compound into the pores of the material) in a proportion 1:5 by weight (named as P-A2 and P-C2 depending on whether the compartment is the anode or the cathode respectively).

The poultice made of long fiber cellulose (Arbocell BC-1000) was chosen due to this material: 1) has large pores than other materials, which allow it to house a greater amount of solution [32,34,68]. This fact favors the wetting of the stone to be treated, and therefore, the dissolution of a greater amount of salts present in its pores, which will be forced to migrate due to the influence of the DC field; 2) stores a greater amount of precursors than other materials such as kaolin and it does not hinder their mobilization as other materials due to its low ion exchange capacity; 3) unlike other poultices such as kaolin, it leaves little residue on the surface of the material; 4) improves the contact between the setup and the surface of the material. This fact, unlike previous electroprecipitation studies, where this cell C3 was filled with a liquid solution [49–51], facilitates the extrapolation of the treatment to real situations where the method must be applied to irregular surfaces, since the loss of liquid that could be in the contact area is reduced. Furthermore, and despite this cellulose poultice, a neoprene gasket was pasted on the edge of the cell C3 to improve the contact between the cell and the stone.

In any case, all poultices used in both compartments will serve as a storage and retention medium for the extracted ions.

2.3. Solutions used to supply the precursors

Applying electrodeposition methods, for the rehabilitation of porous materials, has the advantage that it is possible to carry out an on-demand selection of suitable external solutions to promote the formation of insoluble compounds that are chemically compatible with the material to be treated. This fact is of utmost importance, since a high chemical affinity between the precipitated compound and the treated material ensures that the behavior of both materials will be similar against fluctuations under external conditions, such as temperature and relative humidity. Therefore, considering the chemical composition of both stones (limestone and dolomite), it is intended to precipitate some chemical compounds whose composition belongs to the group of magnesium, calcium, or calcium-magnesium carbonates.

Calcium is not supplied from any compartment to stones to be treated since their initial content was high. This is due to the previous salt contamination to which the specimens were subjected.

Magnesium was supplied from the anode towards the cathode through the stone. To supply this cation, a 0.5 M magnesium acetate solution was used (both in cell C1 and C3). The decomposition of the poultice P-A1 also provides Mg^{2+} ions during the pH buffering process.

Carbonate was supplied from the cathode towards the anode through the stone. Two different solutions, with different initial pH values, have been used to supply it. The pH value will influence in the ionic spice in which this ion is found. The carbonates above a pH value of 10.3 are in the form of carbonate ion (CO_3^{2-}), while those below 10.3 and above 8 the main species is bicarbonate (HCO_3^-). In three specimens per stone, the solution used was 0.5 M ammonium carbonate pH 9 (in this case the setup is named onwards A-M). In the other three specimens, the solution used was 0.5 M sodium carbonate pH 11.8 (in this case the setup is named onwards N-M).

2.4. Electrokinetic procedure

The electrokinetic procedure used in this study is based on the electro precipitation of insoluble inorganic compounds, applying the recently procedure developed in [49–52], in which a more detailed information can be found. This method comprises two steps between which the polarization of the electrodes is reversed and consequently, the relocation of the different elements hosted in every cell (i.e., poultices and solutions) must take place.

During each step, a constant voltage of 27 V was applied (see Fig. 2). This voltage was established on the assumption that the application of a high current density from the beginning of the treatment, in this case a current of about 11–12 mA, should allow a faster mobilization of the anions present inside the stone (i.e., Cl^-, NO_3^- and SO_4^{2-}) than those precursors supplied from the cells (especially those with less mobility, such as the carbonate ion). This fact should facilitate the extraction of salts before the main percolating pathways of the material collapse due to the precipitation of insoluble compounds.

During the first treatment step, it is expected that the current density that flows through the stony material will be high in the beginning, due to the high ionic content that the material presents. In consequence, it is expected that a massive exit of the ions that formed the soluble salts, towards the electrodes of opposite polarity, take place. This mobilization must cause an increase in the ionic content of these ions in the poultices used in each compartment, whereas in the stone a decrease should occur. At the same time, the entry of the ions selected as precursors must take place. Summarizing, during this step it is expected that a substitution of the anions and cations that initially were in each stone specimen by new ones that are supplied from the selected solutions will take place. As precipitation of inorganic compounds begins to occur inside percolating pores, the transport of the electric current by the ions present is hindered. Consequently, the resistance that the material opposes to the current flow will increase and the density of the current flowing will decrease considerably [50].

In addition to the areas where the product has precipitated, other areas within the material will remain enriched with a particular precursor (the area near the anode will be enriched with the supplied cation while the area near the cathode will be enriched with the supplied anion [50]).

At this point, the second treatment step must be applied. During this step, ionic mobilization and rapid precipitation of the inorganic compound to be formed is again expected to take place, since the ions are forced to penetrate into the material through previously enriched zones with the respective counterion [50]. This step will be considered ended when the value of the current density flowing through the material reach a value close to zero.

Between each of the treatment steps, all poultices are renewed by new ones, as well as the solution in contact with each electrode.

All tests lasted 30 days. The duration time of the first step varied between treatments according to the resistance and current measurements recorded (taking as the point of change between steps currents around 1 mA).

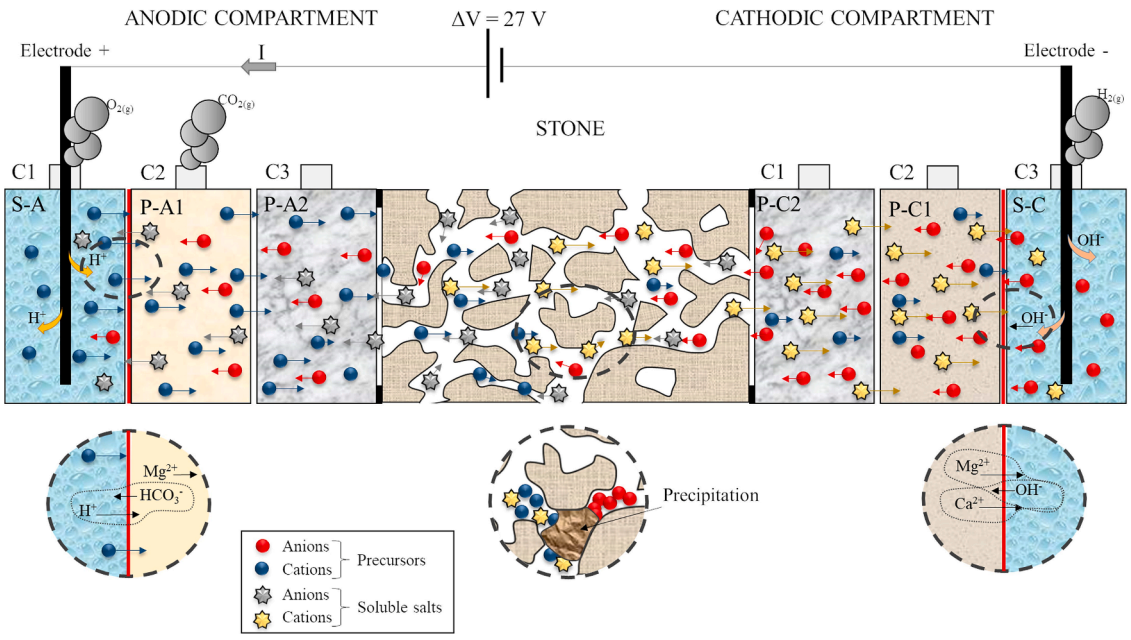


Fig. 2. Schematic diagram of the procedure used to desalinate and consolidate the stone by the electro-precipitation of insoluble inorganic compounds in some pores of the material. In this case only the first step of the treatment is shown. The second step would be similar to this but changing the polarity of the compartments and repositioning poultices and solutions. In addition, the electrochemical and chemical processes that take place throughout the setup are shown in detail, i.e., water electrolysis (showing the generation of H^+ and OH^- on the surface of the electrodes), pH buffering processes (through the poultices and mobilized compounds), and electro-precipitation (when the saturation concentration of certain compounds inside the pores of the material is exceeded).

2.5. Methods applied to assess the treatment effectiveness

As indicated above, two setups, where a different solution that supplies the carbonate ion (i.e., A-M and N-M), have been tested. For each of the setups, three specimens per kind of stone were treated.

During the test, the evolution of the main electrical parameters, i.e., resistivity (in kΩ•m) and current density that flows through the specimens (in $A•m^{-2}$) were recorded. For that purpose, the potential drops between the electrodes hosted in the cells C1 and, in a 1 kΩ resistance, connected in series with the setup, were measured.

At the end of each test, the following parameters were assessed to quantify:

(a) Desalination effectiveness. For this purpose, the anion content (Cl^-, NO_3^-, and SO_4^{2-}), either in poultices or stones specimens, was determined. Both poultices and stone specimens were dried in an oven at 50 °C for 5 days until reaching a constant weight. After that, in the case of each stone specimen, as stated before, the ion content was quantified in the two fragments in which it was segmented. The anion content into the poultices was determined after each treatment step. The rest of the procedure followed to measure the anionic content, by IC, was the same procedure as that explained in section 2.1.

(b) Consolidation effectiveness. For this purpose, the following parameters were assessed to analyze the changes caused, in the pore structure, due to the precipitation of different insoluble compound inside the pores:
- Petrography to assess textural and mineralogical details in transmitted (FBF) and reflected (FDF) light mode using the equipment stated before.
- XRD to identify the mineralogy of the precipitated compounds.
- Pore size distribution and accessible porosity to mercury. This technique was applied, in duplicate, using stone specimens with the same size and equipment as stated before.
- Changes in the P-wave propagation using the same equipment and procedure mentioned above.
- ESEM-EDX techniques to characterize the textural and chemical composition of the compounds precipitated.

(c) Aesthetic risk associated with the technique. For this purpose, the color changes at different stages of the test were calculated in order to measure the changes caused by: the entry of salts (Initial color vs color after salt contamination), the desalination and consolidation of the stones (color after salt contamination vs color after electrokinetic treatment), and the global change of color (Initial color vs color after electrokinetic treatment). For this purpose, the color variations: ΔL^*, Δa^*, Δb^*, ΔC^*, and total color difference (ΔE^*ab), according to the following expression, were calculated.

$$\Delta E^* = [(\Delta L^*)^2 + (\Delta a^*)^2 + (\Delta b^*)^2]^{1/2}$$

where the parameters ΔL^*, Δa^*, and Δb^* show the variation in the lightness values L*, and in the chromatic coordinates a^* (red-green) and b* (yellow-blue).

In addition, to assess the risk associated to the color change, the index proposed by Mokrzycki and Tatol [69] was applied. This index established different levels of color change as a function of the visual color perception of the human eye: $0 < \Delta E^*ab < 1$, the observer does not notice the difference; $1 < \Delta E^*ab < 2$, only an experienced observer can notice the difference; $2 < \Delta E^*ab < 3.5$, an unexperienced observer also notices the difference; $3.5 < \Delta E^*ab < 5$, clear difference in color is noticed; $5 < \Delta E^*ab$, observer notices two different colors.

3. Results and discussion

3.1. Stone properties

Thin section images taken in transmitted (FBF) and reflected (FDF) light of Redueña rock show the typical texture and mineralogic composition of an oolitic dolostone (see Fig. 3). The cross-polarized-transmitted light image (Fig. 3a) shows small spheres of carbonate composition with a variable diameter between 360 and 230 μm dispersed in a dolomicritic matrix. The ooids retain their rounded

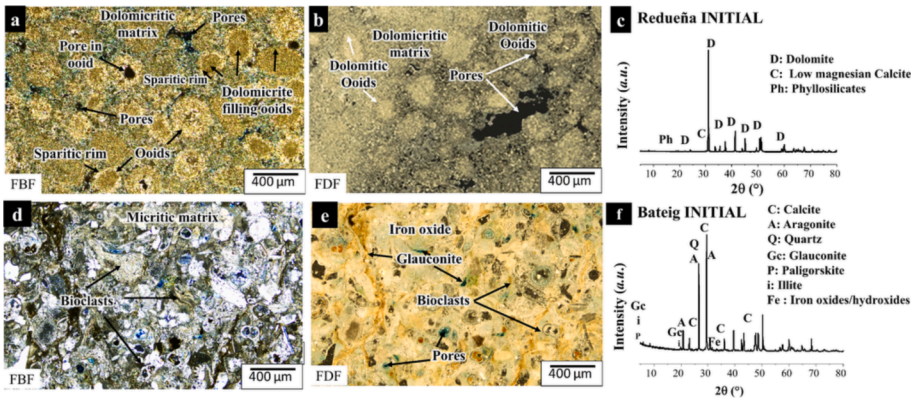


Fig. 3. PLOM images of Redueña (a and b), Bateig (d and e), both before treatment, showing textural and mineralogical details in transmitted (FBF) (a and d) and reflected (FDF) light mode (b and e). Also, XRD profiles of both stones before treatments (c: Redueña and f: Bateig) are shown.

nature, and it is common to distinguish a core made of dolomite and an outer layer of dolosparite. The ooid edge sparitization generally varies in thickness between 30 and 50 µm, although not all suffer the recrystallization. On occasions, the nucleus of the ooids sustained a loss of material, giving rise to rounded pores. Pores also appear in the dolomicritic matrix, generally affecting the space between ooids. Its dimensions fluctuate between a length/width ratio of 110/56 µm, producing vugular porosity by coalescence of pores with sizes that reach a ratio of 360/60 µm.

The reflected light image (Fig. 3b) indicates the presence of vugular pores with an aspect ratio of 825/226 µm. Image contrast shows microcrystalline concentric layers in some ooids. The corresponding X-ray diffraction profile (Fig. 3c) shows the diffraction maxima of dolomite (D), a low shoulder of low magnesian calcite, and weak signals of phyllosilicates.

Regarding Bateig sample, Fig. 3d indicates that this stone is a biomicritic limestone with a high content of sparite recrystallized bioclasts deposited on a micritic matrix, partially affected by iron oxides/hydroxides. Most bioclasts (foraminifera, bivalves, and other mollusks) have variable L/W ratios between 486/131 µm, 119/94 µm, or smaller (49/68 µm). Locally, the skeletal structures form spherical valves (82.7 µm) or elongated (66/63 µm), crystallized with sparite that grows on the outer edge of the shell, reaching a thickness of 21.3 µm. Microfossils appear partially filled with quartz grains (14/14 µm), micrite, or phyllosilicates. A moldic porosity, the most common product of a material loss is identified, whose pores are proportional to the diameter of the nucleus of the bioclasts.

The reflected light image (Fig. 3e) shows details of the bioclasts whose brown coloration in the nucleus indicates a filling of micrite and phyllosilicates, besides light gray growths confirming their microsparitic character of aragonite. Iron oxides produce a yellowish-brown coloration along the surface. Fig. 3f shows the XRD pattern before the treatments indicating intensity peaks of calcite and aragonite, the main components of the original rock, besides that of illite group clays with different hydration degree, Paligorskite and Glauconite, as previously reported [70].

Physical properties data of both stony materials used in this study, before the application of the electrochemical treatment, are summarized in Table 1.

Both stones have high percentages of accessible porosity to water, with Redueña dolostone having the higher of the two. In both materials it is noted that: 1) the accessible porosity to mercury is lower than to water, with a similar percentage value for both stones (15 % approximately). This fact indicates the existence of a pore volume with an access size diameter greater than 360 µm (upper limit of the porosimeter used). 2) There is a high amount of difference between the accessible porosity to water and the capillary porosity (41.3 % for Redueña and 39.7 % for Bateig). This indicates that, in both materials, there is a high volume of pores that are not within the range of pores with capillary access size between 0.1 and 100 µm. 3) The capillary coefficient of Redueña and its absorption dynamics show that this stone absorbs water much faster than Bateig. 4) The saturation degree obtained by both immersion and capillarity for both rocks (around 75 % approximately), indicate that there is a certain volume of pores that are not well communicated, especially in Redueña.

Table 1
Physical properties of Redueña and Blue Bateig.

Parameters	Redueña	Blue Bateig
Water accessible porosity (% v/v)	23.21 ± 2.73	15.74 ± 0.22
Mercury accessible porosity (% v/v)	19.69 ± 1.92	14.25 ± 1.30
Capillary porosity (% v/v)	13.62 ± 1.45	9.49 ± 0.02
Capillary coefficient ($kg/m^2h^{0.5}$)	1.86 ± 0.12	0.31 ± 0.02
Saturation degree by immersion (%)	74.71 ± 2.28	74.76 ± 0.76
Saturation degree by capillarity (%)	71.42 ± 1.97	74.71 ± 0.95
Bulk density (kg/m^3)	2185 ± 77	2279 ± 5
UPV (m/s)	3855 ± 786	3911 ± 41

Regarding the pore size distribution, significant differences are noted between the pore size distributions of both stones (see Fig. 4 and Table 2). Redueña shows a bimodal pore size distribution: a pore range between 0.1 and 3 µm (peaking at 1 µm), and a range of pores between 5 and 50 µm. About 94 % of the total porosity corresponds to pores with an access diameter between 0.1 and 100 µm, i.e., pores of capillary absorption. Only a small fraction of the total porosity (about 1.5 %) lies in the nanometer range. Blue Bateig shows a unimodal pore size distribution with a pore size diameter lower than 5 µm (peaking at 0.2 µm). In this stone, the 60 % approximately lies in the pore range with an access size diameter into the capillary pore range (within this range, 57 % correspond to pores between 0.1 and 1 µm). About 37 % correspond to pores with access diameter lower than 0.1 µm, which are not accessible to water.

The difference observed into the capillary range 0.1–100 µm explains why Redueña absorbs water much faster than Bateig.

After the contamination process with soluble salts, the salinized Redueña sample image, taken in reflected light mode (Fig. 5a), shows a high content of whitish mineralization scattered throughout the entire stone, whose dimensions generally appear in a length/width ratio of 36/18 µm or less. Some of them occupy pores or crystallize at the pore edges. The complete XRD profile in Redueña samples (Fig. 5c) indicates the presence of dolomite diffraction maxima (D) the main component of the dolostone, as well as mineralization resulting from the salinization process, which are visible in the zoom on the right. The salt mineralizations identified are potassium nitrate (Niter), gypsum, halite with some content of potassium; and hydrated Mg-Ca-K sulfate, known as

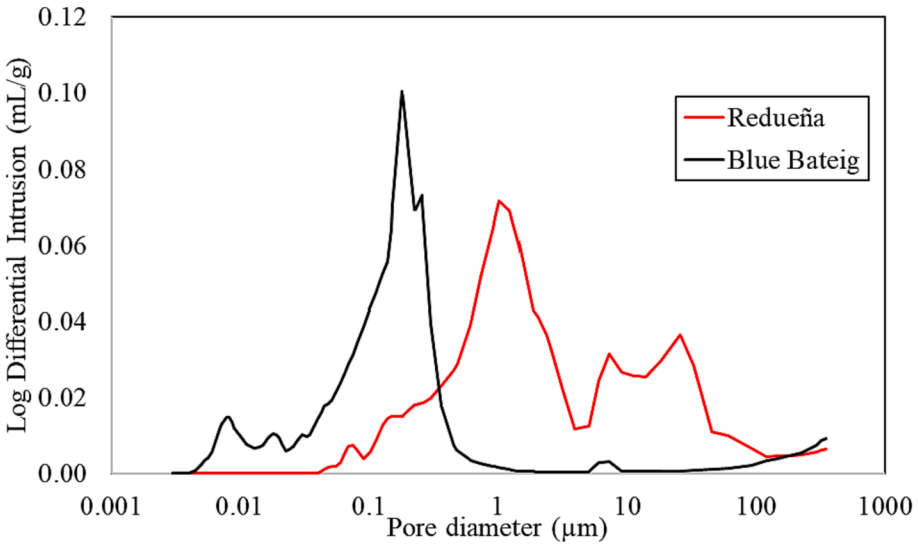


Fig. 4. Average pore size distribution (n = 2) of stone specimens: Redueña (red line) and Bateig (black line). (For interpretation of the references to color in this figure legend, the reader is referred to the web version of this article.)

Table 2
Intruded mercury volumes for different pore size ranges (in mL/g and %) for both treated and untreated stony materials: Redueña and Blue Bateig. The mercury accessible porosity (MAP), and its variation with respect to the initial porosity (Δ) are also shown.

Stone	Total intruded volume (mL/g 10^3)	Pore size ranges (μm)					MAP (%) [Δ]	
		<0.1	0.1–1	1–10	10–100	>100		
Redueña	78.13	1.23	26.09	33.39	14.43	3.00	19.70	
A-M	71.35	0.00	5.97	28.22	35.32	1.84	15.54	[-21.12 %]
N-M	66.60	0.00	0.04	26.69	36.56	3.31	14.33	[-27.26 %]
Blue Bateig	60.68	22.76	34.64	0.66	0.74	1.88	14.25	
A-M	60.28	21.63	36.81	0.66	0.48	0.69	13.40	[-6.0 %]
N-M	50.24	25.17	23.33	0.40	0.40	0.94	11.96	[-16.1 %]
Stone	**Total intruded Volume (%)**	**<0.1**	**0.1–1**	**1–10**	**10–100**	**>100**		
Redueña	–	1.56	33.76	43.05	17.69	3.94		
A-M	–	0.00	8.37	39.55	49.51	2.58		
N-M	–	0.00	0.06	40.08	54.89	4.97		
Blue Bateig	–	37.51	56.93	1.09	1.22	3.09		
A-M	–	35.89	61.10	1.09	0.80	1.15		
N-M	–	50.10	46.44	0.80	0.80	1.87		

polyhalite.

The salinized Bateig sample, taken in reflected light (Fig. 5b), shows the presence of microcrystalline and submicron salts, light in color, dispersed throughout the micritic matrix, with sizes between 26.46/21.45 μm and 12.64/14 μm. The pores are moldic in nature with dimensions around 41/39 to 45/20 μm. The diffractograms of this stone (Fig. 5d) indicate the maxima intensity of calcite (C), aragonite (A), and quartz (Q), which are the main components of this stone. In addition to the main phases, signs of potassic halite, polyhalite, halite, hydrated calcium sulfate and potassium nitrate (niter) appear after salinization.

This high salt content after the contamination process and its identification were corroborated by SEM-EDX results (see Fig. 6). The salt effect appears more dispersed on the Redueña matrix than that of the Bateig. While an inhomogeneous, less thick, and less extensive layer crystallized in Redueña, a very defined layer of crystals developed in Bateig. This behavior could be related to differences in adherence between the two stone surfaces, considering the pore structure of the original stone. In the case of Redueña, the higher accessible porosity, the intercrystalline porosity developed between the dolomite crystals, in addition to its surface roughness, due to its non-planar texture produced by anhedral and curved dolomite crystals, and microporosity within the crystals themselves facilitated the deposition and penetration of salts [71,72]. In contrast, in the case of Bateig, adhesion was different since the reduced intergranular porosity with the calcite resulted in a thick superficial crust of well-defined crystals.

3.2. Desalination treatment. Effectiveness

3.2.1. Salt content in stone samples

Before applying the treatment (see Table 3), the anion content inside both stony materials exceeded the upper concentration limit established by the Austrian standard ÖNORM B [73], (in %g/g, Cl^-: 0.10, NO_3^-: 0.15, and SO_4^{2-}: 0.25). Especially in Redueña, which, due to its greater porosity, has absorbed a higher content of salts. Attending to this standard, this high initial anion content involves a serious risk for a porous building material. For this reason, an active desalination intervention must be applied.

At the end of the treatment, the reduction in the anion content achieved in all cases, regardless the stone and the precursors mobilized, was significant. The reduction achieved in the most mobile anions, such as chloride and nitrate, was 100 %. In the case of the least mobile anion, in this case sulfate, the reductions achieved in the most porous material (i.e., Redueña) were 100 %; while in Bateig the reductions achieved were above 90 %. In any case, the content remaining in all the treated specimens is so low (lower than the bottom concentration limit established by the standard ÖNORM B, in %g/g, Cl^-: 0.03, NO_3^-: 0.05, and SO_4^{2-}: 0.1) that it does not pose a risk to the material.

Regarding cations, there is a considerable reduction of Na^+ and K^+

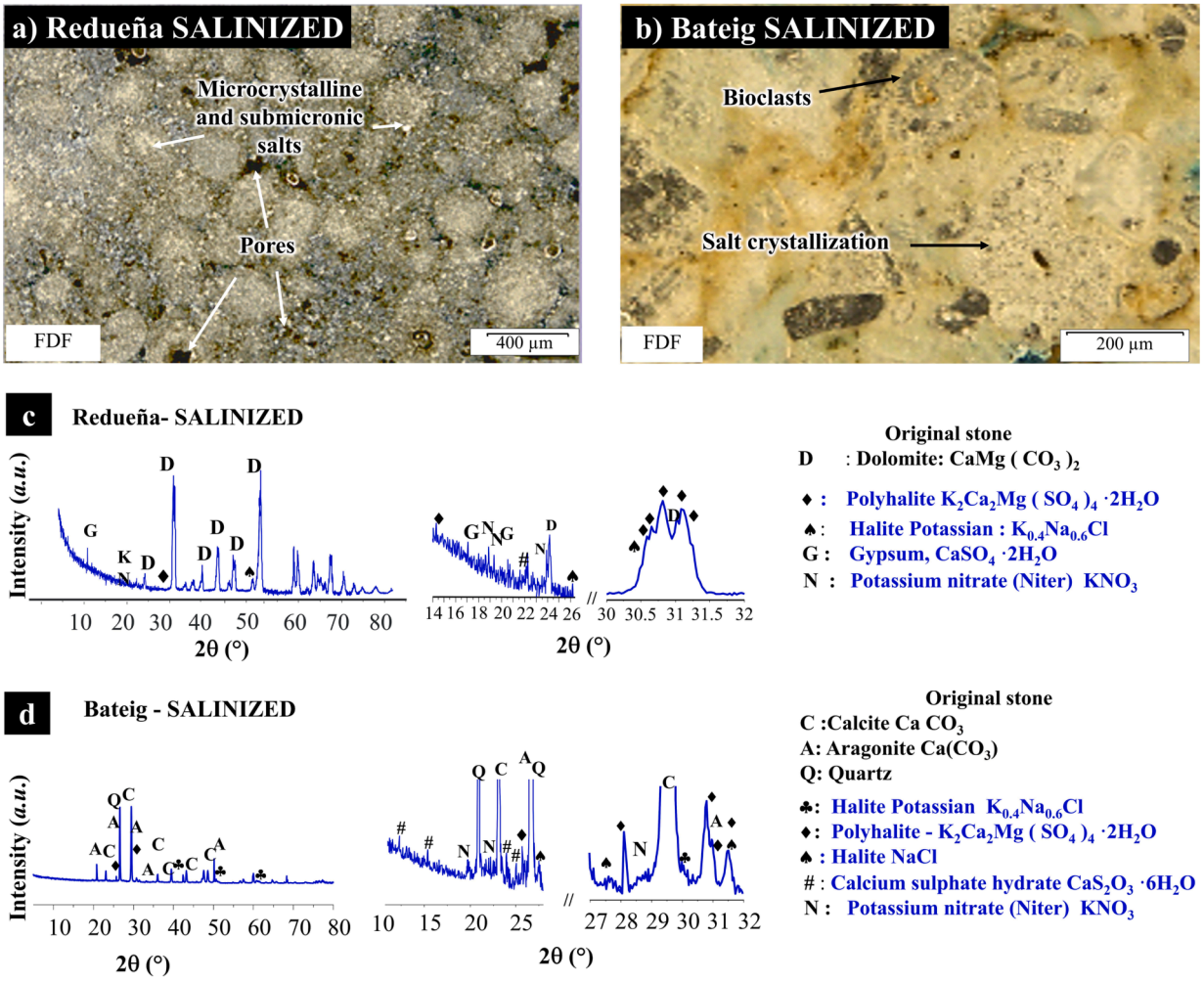


Fig. 5. PLOM images of both salinized stones (a: Redueña and b: Bateig), in reflected (FDF) light mode. Also, XRD profiles of both stones after the salinization process and before treatments (c: Redueña and d: Bateig) are shown. Zoom details showing the peaks associated with the crystallized salts are shown to the right of the main diffractogram.

(100 % in all cases regardless of the stone) and a smaller reduction of Ca^{2+} (about 66 % in Redueña and 45 % in Bateig). In the case of Mg^{2+}, there is a considerable increase due to the mobilization of this cation during the treatment and its subsequent precipitation into the stone.

3.2.2. Salt content in the poultices

The analysis of the mobilization of the main anions during the treatment, based on the anion content retained in the different poultices used in each of the two steps of the treatment (see Table 4), shows that the extraction of these anions occurred preferably during the first step of the treatment. This high extraction rate during the first step may be related to its duration (between 11 and 25 days depending on the porosity of the material). The higher the porosity of the material, the longer the time spent in the first step of the treatment. Previous studies carried out on other materials [66,67] have shown that with a shorter time interval, approximately one week, similar reduction percentages can be achieved.

The data collected in this table indicate that during treatment the anions are preferentially mobilized towards the anode, especially anions with greater mobility, such as chloride and nitrate. This fact indicates that the mobilization of ions under the influence of an electric field is higher to the mobilization of ions by other processes such as diffusion and advection, as already demonstrated [74]. This study shows that the diffusion coefficient of an ion is at least an order of magnitude lower than its ionic mobility under the influence of an electric field. Furthermore, considering that the influence of the pore network in both transport mechanisms is similar, it is estimated that for a charge species the ion mobility is 40 times the charge on the species higher per volt applied than the diffusion coefficient for the same species. Taking this into account, for the monovalent chloride ion, under the conditions of this study (27 V), the mobility will be 1080 times higher.

3.3. Consolidation treatment

3.3.1. Petrography

After the A-M treatment, Redueña sample observed by reflected light (see Fig. 7a) shows mineralization at the edges of ooids and pores identifiable by a pale-yellow contrast. Epitaxial growth around the pore edges is widespread, although it does not occur in all pores. The mineralization occupies a thickness between 25 and 40 µm, sometimes reaching 60 µm. XRD results (see Fig. 8a, red line) indicate the crystallization of two types of carbonates after A-M treatment, Mg and Ca hydroxide carbonate and Mg-rich dolomite, described below. The presence of pores, in general, consists of inhomogeneous pores in dimensions ranging from larger pores that reach up to 260/125 to 280/235 µm, intermediate pores from 178/105 to 160/78 µm, and tiny pores of 55/ 44 µm.

The A-M treatment in Redueña stands out for not having peaks corresponding to the crystallized salts, with dolomite signals being equally predominant. However, some additional diffraction maxima

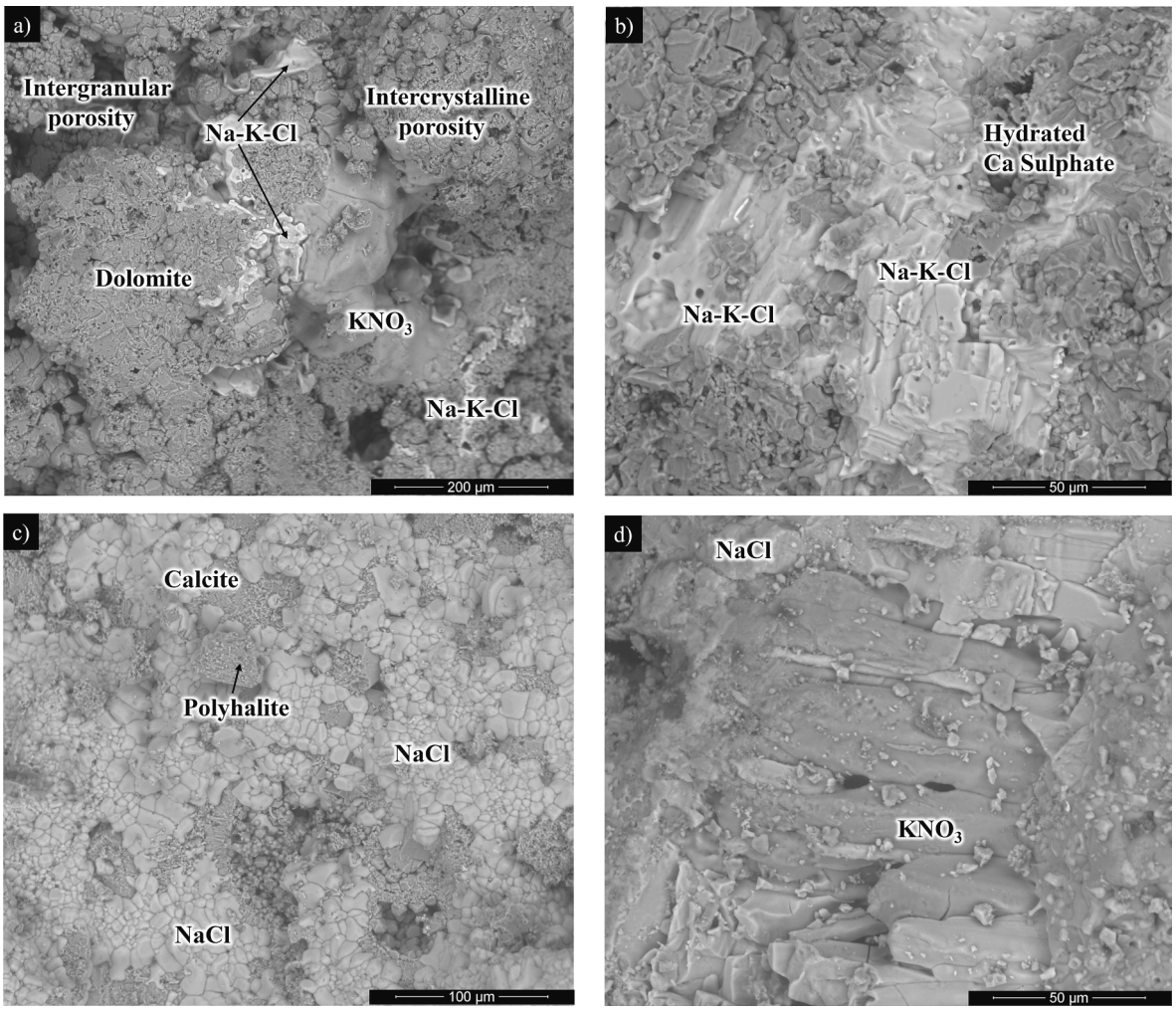


Fig. 6. SEM micrographs of both salinized stones, Redueña (a and b) and Bateig (c and d) in BSE mode.

appear corresponding to carbonate hydroxide hydrate, with a high agreement with Sergeevite, a calcium Mg carbonate hydrate, with general formula $CaMg_{11}(CO_3)_{13}{\cdot}10H_20$ which has variable water content and CO_3/OH ratio, according to the formula $Ca_2Mg_{11}(CO_3)_{13\text{-}x}(HC0_3)_x(OH)_x{\cdot}(10\text{-}x)H_2O$, where $x \leq 4$, [75]. Additionally, it is present a magnesium-calcium carbonate richer in magnesium known as Huntite ($Mg_3Ca(CO_3)_4$), which can appear simultaneously with Sergeevite [75,76].

After the N-M treatment, there is no evidence of mineralization similar to that identified in the A-M Redueña samples, as shown in the reflected light image (see Fig. 7b). Only appear visible areas with clear contrast whose dimensions fluctuate between 36/19 µm and 41/16 µm or as individual crystals occupying pores or regions of higher concentration There is generally a reduction in the pores with sizes of 286/130 to 319/135 µm. After this treatment, the XRD profile indicates different additional signals (Fig. 8a, green line), such as the main diffraction maximum of the calcium-rich dolomite (toward the left of the profile). In addition, the profile shows the diffraction maximum of magnesium-enriched dolomite, whose 2-theta tends toward the greater angles. Besides, with less intensity, additional peaks corresponding to the Huntite appear (Table S1 summarizes the minerals identified in Redueña dolostone by XRD and their specifications).

Regarding Bateig, after A-M treatment (Fig. 7c), the reflected light image indicates a new whitish-yellow mineralization of 136/118 µm, which could correspond to the Ca carbonate hydroxide identified by XRD (Fig. 8b, red line). Bioclast pores are affecting the matrix, some filled with phyllosilicates with an average size of 120/82 µm. The diffractogram shows, in addition to the presence of calcium carbonate hydroxide, a metastable phase among the hydrated calcium carbonate [77], magnesium calcite, whose main peak shifts to the right due to an increase in Mg content, and the metastable calcium carbonate polymorph known as vaterite, which can crystallize in environments with a pH similar to that of the current experimental conditions of the A-M treatment [78].

The reflected light image corresponding to the N-M treatment applied in Bateig (Fig. 7d) shows a well-compacted calcitic matrix with a few pores with sizes between 107/96 and 162/130 µm. A yellowish-white mineralized zone could correspond to high magnesium calcite, as identified by XRD (Fig. 8b, green line), in which two types of intensity maxima correspond to calcite, showing different Mg/Ca ratios: Ca-rich calcite, and Mg-rich calcite. (Table S2 summarizes the minerals identified in Bateig biomicritic limestone by XRD and their specifications).

3.3.2. *Physical changes into the pore structure*

The changes caused in the pore network (see Table 2 and Fig. 9) show that both treatments, regardless of the stone, reduce the accessible porosity to mercury. These reductions were more pronounced in Redueña, which seems to indicate that the higher porosity caused a greater accumulation of ions within the pores before the collapse of the vast majority of the percolating pores took place. Although it may also be influenced by the longer treatment time required by this stone during the first step (around 20–25 days for Redueña, and 15–20 days for Bateig), since, as mentioned above, the higher the porosity, the longer the time needed to fill the pores.

Table 3
Initial and final average ion content in both stones treated with different anion precursors (A-M: ammonium carbonate; N-M: sodium carbonate). Values are expressed in % g/g, referred to the dry weight of the stone. Also, the desalination effectiveness in % (E-%) is expressed.

Redueña	A-M						
	Cl^-	NO_3^-	SO_4^{2-}	Na^+	K^+	Ca^{2+}	Mg^{2+}
Initial	0.74 ± 0.44	1.10 ± 0.62	0.50 ± 0.18	0.64 ± 0.32	0.86 ± 0.20	0.08 ± 0.00	0.04 ± 0.00
Final	0.00 ± 0.00	0.00 ± 0.00	0.00 ± 0.00	0.00 ± 0.00	0.00 ± 0.00	0.03 ± 0.01	0.30 ± 0.12
E-%	100	100	100	100	100	66.67	–
	N-M						
Initial	0.74 ± 0.44	1.10 ± 0.62	0.50 ± 0.18	0.64 ± 0.32	0.86 ± 0.20	0.08 ± 0.00	0.04 ± 0.00
Final	0.00 ± 0.00	0.00 ± 0.00	0.00 ± 0.00	0.00 ± 0.00	0.00 ± 0.00	0.03 ± 0.01	0.19 ± 0.10
E-%	100	100	100	100	100	68.18	–
Bateig	**A-M**						
	Cl^-	NO_3^-	SO_4^{2-}	Na^+	K^+	Ca^{2+}	Mg^{2+}
Initial	0.48 ± 0.08	0.78 ± 0.08	0.29 ± 0.11	0.42 ± 0.03	0.46 ± 0.08	0.12 ± 0.03	0.00 ± 0.00
Final	0.00 ± 0.00	0.00 ± 0.00	0.02 ± 0.01	0.00 ± 0.00	0.00 ± 0.00	0.07 ± 0.03	0.12 ± 0.04
E-%	100	100	93.12	100	100	44.44	–
	N-M						
Initial	0.48 ± 0.08	0.78 ± 0.08	0.29 ± 0.11	0.42 ± 0.03	0.46 ± 0.08	0.12 ± 0.03	0.00 ± 0.00
Final	0.00 ± 0.00	0.00 ± 0.00	0.01 ± 0.01	0.00 ± 0.00	0.00 ± 0.00	0.06 ± 0.01	0.05 ± 0.00
E-%	100	100	97.42	100	100	48.08	–

Between treatments, the reduction was greater in the N-M treatments than in the A-M treatments, which may be related to the ionic form in which the carbonate ion was supplied, which is dependent on the pH of the solution. In this sense, it seems that the yield of the process is higher when the carbonate is supplied as carbonate ion (case N-M) and not as bicarbonate (case A-M).

With respect to the pore sizes that are most affected by this process, it can be seen that the reductions caused are different depending on the material treated. In Redueña, there is a considerable reduction in the volume of pores with access size below 3 μm, especially in pores below 1 μm. In addition, there is an increase in the volume of pores between 3 and 25 μm in size, probably caused by a displacement of the pore volume when the pores that initially had a larger initial size were partially filled, or by the presence of new pores not filled by the treatment that appeared after the damage caused by the salts. In Bateig, the reduction affects the larger pores, above 0.1 μm, and increases the volume of pores with access size below 0.1 that are not accessible to water. This result is similar to that observed in a previous work carried out on quartz-sandstone [51].

The reductions caused in the pore network are also evident in the ultrasonic transmission measurements (see Table 5). In the treated samples there is an increase in UPV, which is more marked in the N-M samples (which indicate a greater filling of the pores and a lower porosity), and especially in Redueña, where the waves even travel much faster than in a less porous material such as Bateig (this fact depends both on the density of the minerals that make up the rock and on the minerals precipitated inside, since the higher the density, the higher the ultrasound transmission [79], in this sense $CaCO_3$ 2.71 g/cm^3 and MgCa$(CO_3)_2$ 2.85 g/cm^3). In summary, the treatment has modified the mechanically useful skeleton of both stony materials, so that the higher the ultrasonic transmission, the higher the mechanical properties of the material, as can be seen from the UCS data.

3.3.3. *Morphology of the precipitated compounds*

Figs. 10 and 11 show SEM micrographs and EDX analysis performed on cross-sections of Redueña and Bateig respectively, treated with each of the aforementioned treatments (A-M and N-M).

In both stones, regardless of the material treated, it can be seen how a filling of the pores with minerals with different crystallography is produced, with similar results to those achieved in previous studies [51,52,80].

SEM-BSE images of Redueña dolostone after A-M treatment (Fig. 10a) show Huntite crystals with columnar habit (210/78 μm aspect ratio) arranged radially on the dolomicritic matrix. Crystallization occupies a large part of the pore space, leaving only 46/21 μm pores. Internally, an intergranular porosity develops whose thickness does not exceed 1 μm. Tiny rhombohedral crystals and concretions corresponding to Sergeevite, whose dimensions do not exceed 18/17 μm, are associated with Huntite. In addition, it is observed a new mineralization of well-defined Magnesium rich dolomite crystals (29/19—–24/15 μm) filling the pore space. The matrix consists of dolomite grains with corroded edges indicating dissolution processes, whose dimensions typically have a fluctuating L/W aspect ratio between 15/13 μm and 12/6.7 μm. The matrix is affected by two kinds of porosity, an intercrystalline (9/3–5/3 μm L/W aspect ratio) porosity and an additional intercrystalline (6.5/

Table 4
Anion content, expressed in % g/g, retained in each of the poultices used in each treatment (A-M and N-M) and at each step (1st and 2nd).

			REDUEÑA			BLUE BATEIG		
	Poultice	**Step**	Cl^-	NO_3^-	SO_4^{2-}	Cl^-	NO_3^-	SO_4^{2-}
A-M	P-A1	1st	0.05 ± 0.05	0.06 ± 0.06	0.01 ± 0.01	1.92 ± 0.31	3.10 ± 0.52	0.47 ± 0.09
	P-A2		0.10 ± 0.06	0.12 ± 0.07	0.02 ± 0.00	1.64 ± 0.25	3.22 ± 0.42	0.66 ± 0.06
	P-C2		0.00 ± 0.00	0.00 ± 0.00	0.00 ± 0.00	0.00 ± 0.00	0.01 ± 0.02	0.07 ± 0.07
	P-C1		0.00 ± 0.00	0.00 ± 0.00	0.00 ± 0.00	0.00 ± 0.01	0.00 ± 0.00	0.01 ± 0.00
	P-A1	2nd	0.00 ± 0.00	0.00 ± 0.00	0.00 ± 0.00	0.03 ± 0.01	0.20 ± 0.06	0.49 ± 0.45
	P-A2		0.01 ± 0.01	0.01 ± 0.01	0.01 ± 0.01	0.02 ± 0.01	0.15 ± 0.06	0.55 ± 0.37
	P-C2		0.00 ± 0.00	0.00 ± 0.00	0.01 ± 0.01	0.00 ± 0.00	0.00 ± 0.00	0.01 ± 0.02
	P-C1		0.00 ± 0.00	0.00 ± 0.00	0.00 ± 0.00	0.00 ± 0.00	0.00 ± 0.00	0.00 ± 0.00
	Poultice	**Step**	Cl^-	NO_3^-	SO_4^{2-}	Cl^-	NO_3^-	SO_4^{2-}
N-M	P-A1	1st	0.27 ± 0.13	0.54 ± 0.28	0.13 ± 0.04	0.83 ± 0.41	1.91 ± 0.56	0.96 ± 0.09
	P-A2		0.82 ± 0.36	1.54 ± 0.88	0.55 ± 0.04	1.21 ± 0.21	2.98 ± 0.12	1.52 ± 0.31
	P-C2		0.00 ± 0.00	0.00 ± 0.00	0.01 ± 0.01	0.01 ± 0.01	0.01 ± 0.02	0.04 ± 0.01
	P-C1		0.00 ± 0.00	0.00 ± 0.00	0.01 ± 0.01	0.00 ± 0.00	0.00 ± 0.00	0.02 ± 0.01
	P-A1	2nd	0.00 ± 0.00	0.00 ± 0.00	0.00 ± 0.00	0.00 ± 0.00	0.01 ± 0.00	0.01 ± 0.00
	P-A2		0.02 ± 0.00	0.00 ± 0.00	0.00 ± 0.00	0.00 ± 0.00	0.01 ± 0.00	0.01 ± 0.01
	P-C2		0.00 ± 0.00	0.00 ± 0.00	0.01 ± 0.00	0.00 ± 0.00	0.00 ± 0.00	0.02 ± 0.00
	P-C1		0.00 ± 0.00	0.00 ± 0.00	0.01 ± 0.00	0.00 ± 0.00	0.00 ± 0.00	0.02 ± 0.00

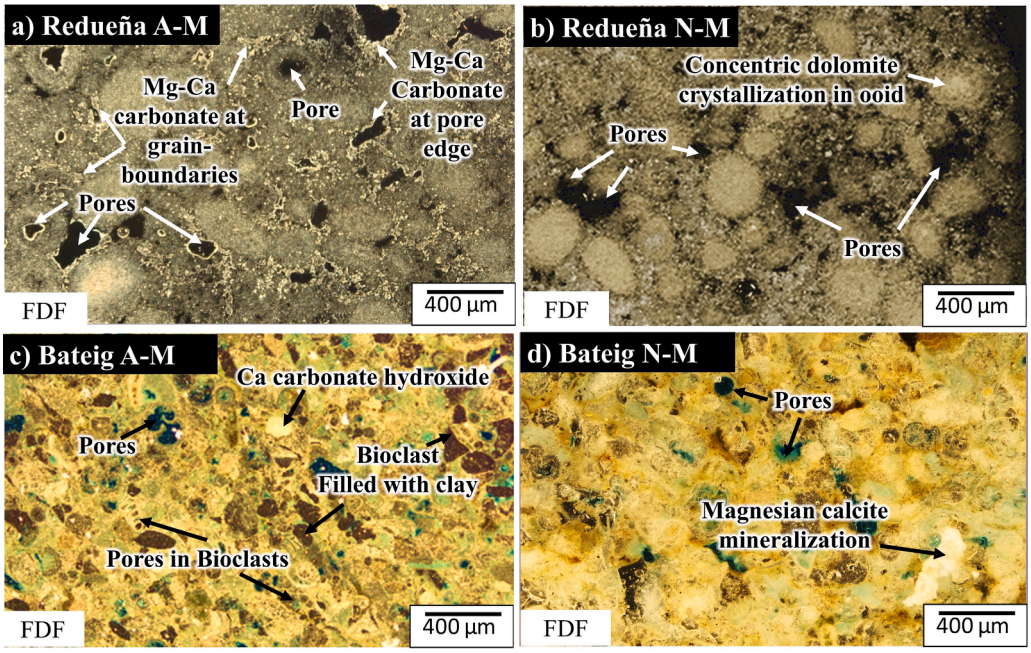


Fig. 7. PLOM images of Redueña (a and b) and Bateig (c and d) after treatments showing textural and mineralogical details in reflected (FDF) light mode.

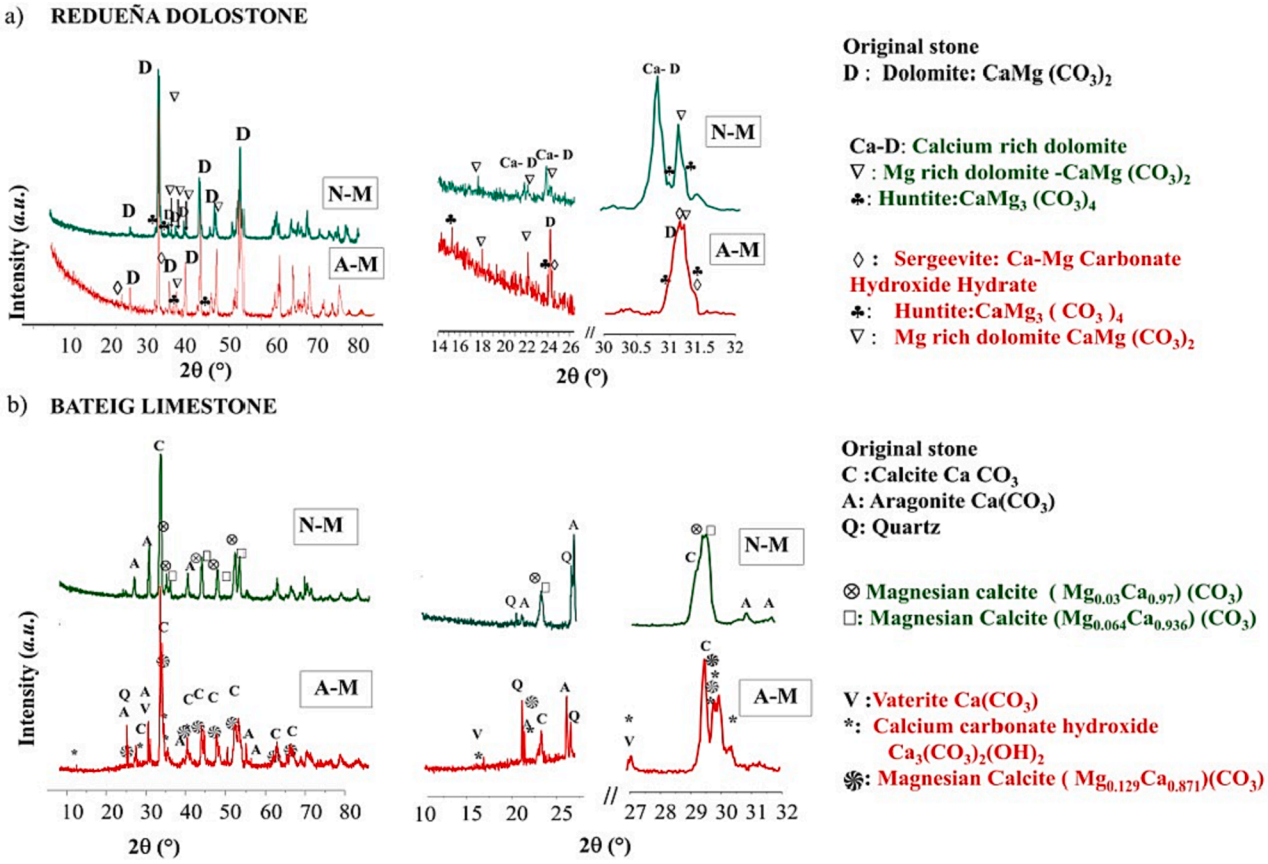


Fig. 8. XRD patterns both of Redueña and Bateig for each treatment A-M (red) and N-M treatments (green). b) Zoom details showing the peaks associated with the compounds precipitated are shown to the right of the main diffractogram. The corresponding symbols and formulas of each compound are summarized at right. (For interpretation of the references to color in this figure legend, the reader is referred to the web version of this article.)

4.5 µm L/W aspect ratio) porosity. The elemental mappings attached to the image show the Mg and Ca distribution in the studied region. The enlarged image (Fig. 10b) allows observing a reduced space with the grain boundaries of the matrix from 7/4 µm to 6/3.8 µm in the zones where the Huntite crystallizes and micropores in the Sergeevite crystals and concretions (12/5—2.3/1.7 µm).

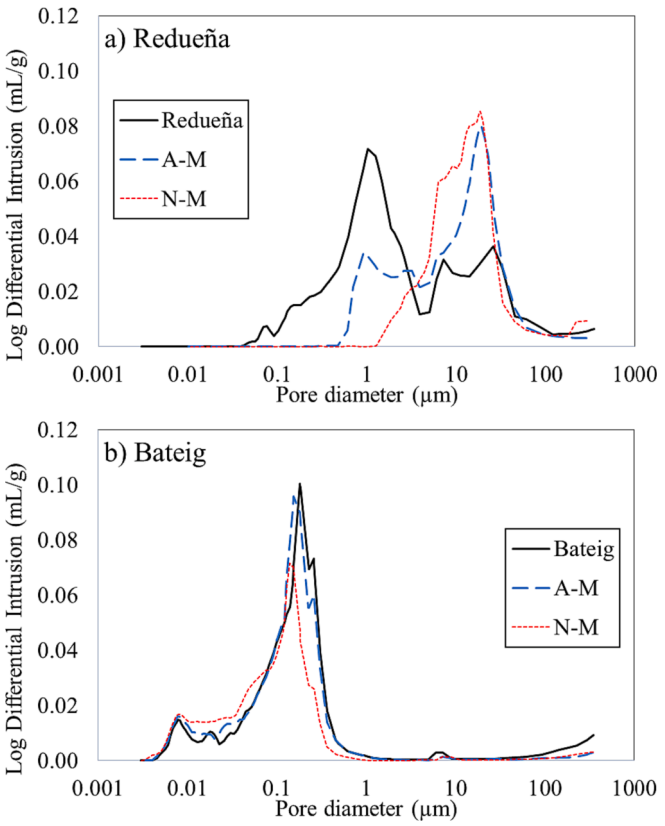


Fig. 9. Pore size distribution of both treated stones, Redueña (a) and Bateig (b) with different precursors: A-M (dash blue line) and N-M (dotted red line). The untreated pore size distribution is also shown (black solid line). (For interpretation of the references to color in this figure legend, the reader is referred to the web version of this article.)

Table 5
Ultrasonic Pulse Velocity (UPV, m/s) of each stone at different times and the variation caused concerning the untreated stone (Δ, in %). Also shown is the uniaxial compressive strength estimated using the mathematical model proposed by [65].

REDUEÑA	UPV (m/s) [Δ]	UCS (MPa)	BLUE BATEIG	UPV (m/s) [Δ]	UCS (MPa)
Initial	3855 ± 786	34.1	**Initial**	3911 ± 41	35.0
Salinized	3773 ± 651 [-2.1]	32.8	**Salinized**	3974 ± 24 [+1.6]	36.0
A-M	4232 ± 92 [+9.8]	40.1	**A-M**	3987 ± 48 [+2.0]	36.2
N-M	4910 ± 414 [+27.4]	50.9	**N-M**	4381 ± 21 [+12.0]	42.5

Fig. 10 c and d correspond to Redueña dolostone after N-M treatment, showing the process of dissolution and enrichment in Ca of the dolomite. In this case, the BSE image shows crystals with a lighter shade of gray on the dolomicritic matrix, which locally occupies surfaces of 90/40–100/70 μm, filling the pore space. The crystals appear locally developing parallel surfaces with curved morphology. The EDS spectra confirm the Ca enrichment of the dolomite. The dolomicritic matrix presents crystals with corroded edges of 7/5 μm with a reduction in the intercrystalline space whose thickness varies between 0.7 and 1.6 μm. In addition, there is a noticeable reduction in the presence of intercrystalline pores, which do not exceed diameters of 1.7/1.4 μm. In the sectors where dolomite dissolution and Ca enrichment do not occur, there is a disaggregation of dolomite, locally developing variable intergranular spaces between 19.5/4.5 μm and 24/13 μm.

Fig. 10d shows the Huntite's disposition over the dolostone's pore space after N-M treatment. The BSE image shows growth of columnar crystals with a darker gray tone formed by individual fibers of 100/3.2 μm, displaying fans that occupy surfaces of 111/50 μm and fill the pores. Locally, occasional pores with dimensions of 79/32 μm and 38/25 μm appear. Furthermore, the stacking between the fibers generates an intercrystalline porosity with a thickness of around 1.12 μm.

Regarding Bateig, the SEM-BSE images corresponding to A-M treatment (Fig. 11a) show the growth of mineralization rich in Mg with darker shades of gray, the result of the increase in the Mg/Ca ratio giving rise to calcite enriched in Mg, previously identified by XRD (Fig. 8b). The BSE image shows clusters of individual crystals of 8/7.5 μm, occupying a surface area of 64/25 μm. The micritic matrix consists of grains of 0.9/0.5 μm with occasional disaggregation of 1.8/1.38 μm. Occasionally, spherules of vaterite (5.2/4.7 μm) appear scattered on the matrix and euhedral crystals of calcite (16/13 μm). Intergranular pores are occasional and develop surfaces of 4/3 μm-7/4 μm. At the same time, intercrystalline porosity affects the micritic matrix, forming surfaces less than 1.8/0.9 μm.

The enlarged BSE image of the magnesium-enriched zone (Fig. 11b) shows a gray tone contrast, indicating fluctuations in the Mg content. An internal zone (medium-grey tone) corresponds to crystals with L/W 31/19 μm aspect ratio, which internally develops moldic microporosity by material loss. Besides, the external region (darker grey tone) includes Mg rich mineralization sometimes showing crystalline faces and extending surfaces, covering areas previously affected by pores. The intergranular porosity shows a reduced thickness of 1.48–5.5 μm.

After N-M treatment, the SEM-BSE image of the Bateig limestone (Fig. 11c) shows calcite crystals with low Mg signal occupying the pore's surface whose dimensions reach a L/W ratio of 114/111 μm. Locally, the space between the crystal and the grain boundary of the micritic matrix generates an intergranular porosity with thicknesses around 0.98—1 μm, and occasional pores whose dimensions are less than 12.7/3.6 μm. In addition, the low Mg calcite develops inter-crystalline porosity with a face-to-face spacing of 2.2–0.6 μm. Bright grains of iron hydroxides (2.4/1.5 μm) and laminar clay minerals (4.8/0.6–2.7/0.4 μm) appear dispersed over the micritic matrix, both inherent to the source rock. The corresponding EDS spectrum confirms the chemical composition of the studied region.

Fig. 11d after N-M treatment shows a well-compacted and slightly porous zone of limestone where two rhombohedral crystals of calcite with a high Mg content (35/44 and 43/22 μm) appear on the micritic matrix as confirmed by the EDS spectrum. The intergranular porosity is low, developing porous surfaces that do not exceed 0.5 to 1.1 μm in thickness. Internally, the newly-formed high Mg calcite crystals have intra-crystalline pores (2.49/1.7 μm). In addition, some calcium carbonate grains (17/8 μm) show corroded edges, indicating dissolution processes. Locally, iron hydroxides/oxides (3.4/3 μm) and phyllosilicates of 3.3/0.8 μm occur dispersed in the matrix. The clay minerals appear intermixed with micritic grains of calcitic composition.

3.4. Color changes

From the data shown in Fig. 12 and in Table 6, it can be observed that the main color changes in both stones were produced due to the salt contamination process (1 vs 2), reaching global color changes (ΔE^*ab) greater than 10, especially in the case of Blue Bateig. In both stones the entrance of salts caused a decrease in luminosity and changes in the chroma that mainly affected the b* coordinate (in this case the changes were qualitatively different depending on the stone, positive in Redueña and negative in Blue Bateig).

After applying the treatment (2 vs 3), a positive change in luminosity was observed in all cases, regardless of the stone and the precursors used. This change counteracts the initial change caused by the entry of salts. Regarding the chroma, the changes detected were different depending on the type of stone: In Redueña the treatment caused changes in the chroma that oppose to those caused during the entry of

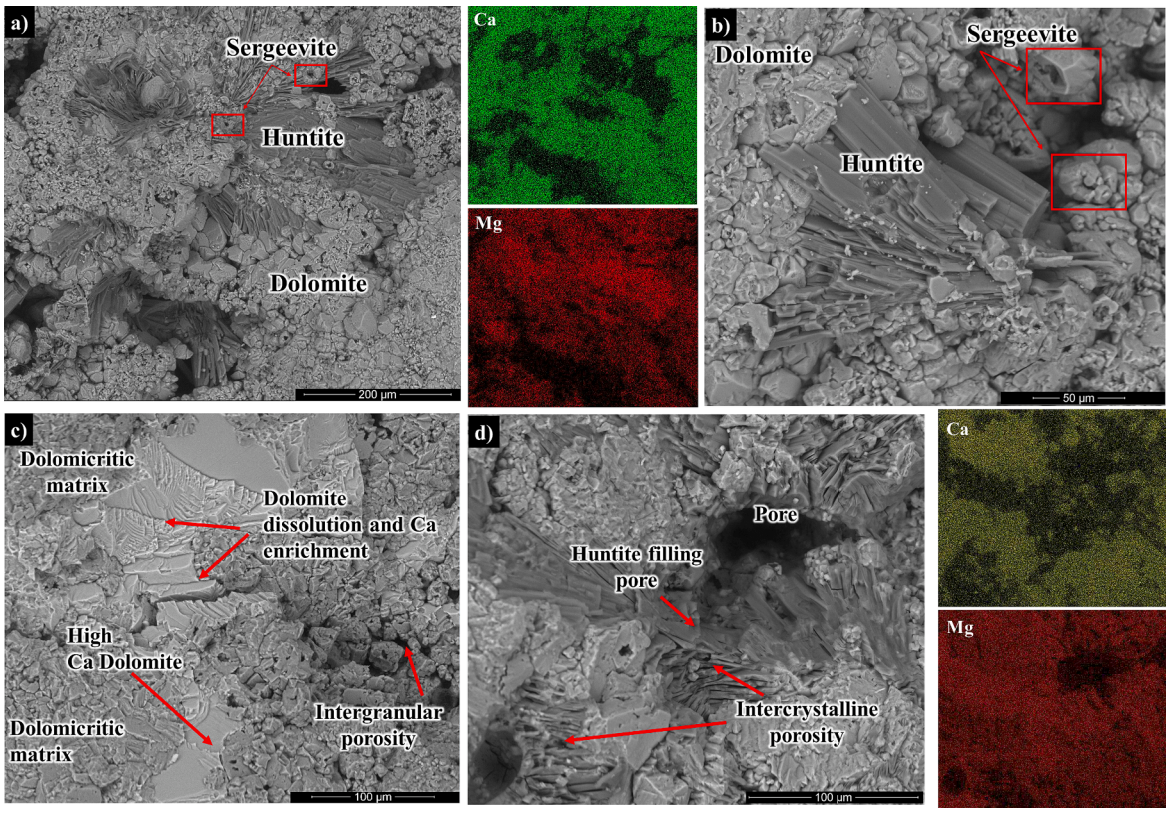


Fig. 10. SEM micrographs of the consolidated Redueña treated with A-M (a and b), and N-M (c and d) in BSE mode. Also, the corresponding EDX mapping of Mg, Ca for each treatment is shown.

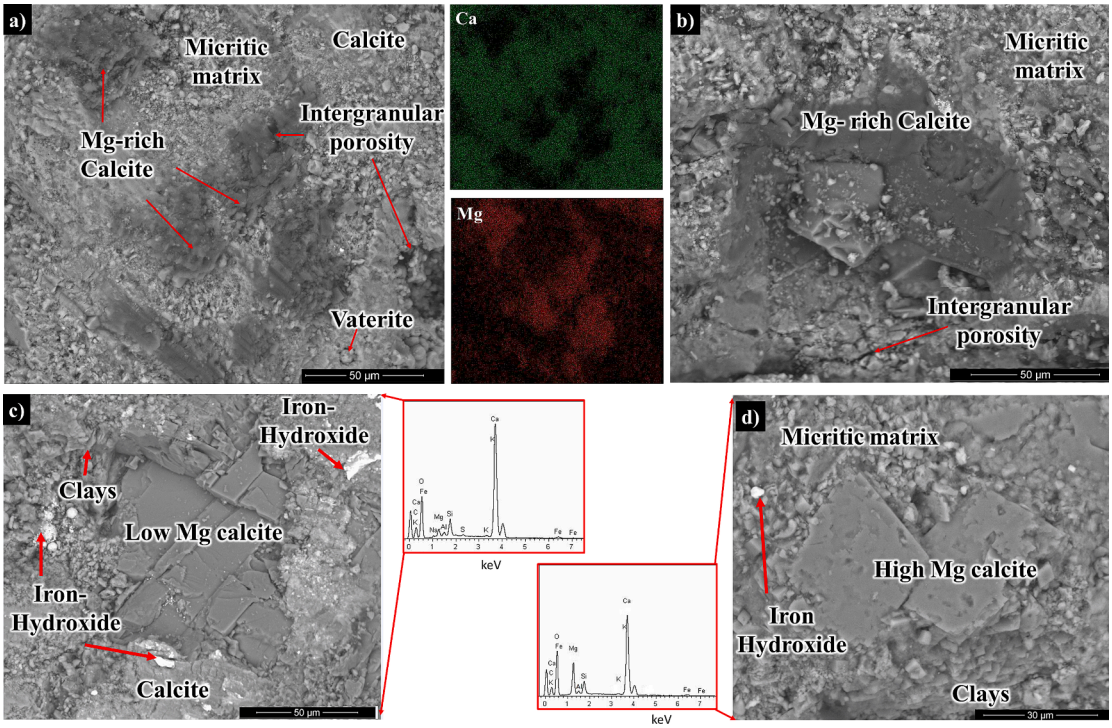


Fig. 11. SEM micrographs of the consolidated Bateig treated with A-M (a and b), and N-M (c and d) in BSE mode. Also, the EDX mapping of Mg, Ca of A-M and EDX analyses of N-M treatment is shown.

salts. However, in Bateig the changes in the chroma were qualitatively similar; this means that the distance in the chroma between the treated and untreated stone was increased.

The global analysis of the changes caused in the surface of the treated specimens (1 vs 3) shows that the total color changes caused by the treatment were greater in Bateig, which could indicate that the risk

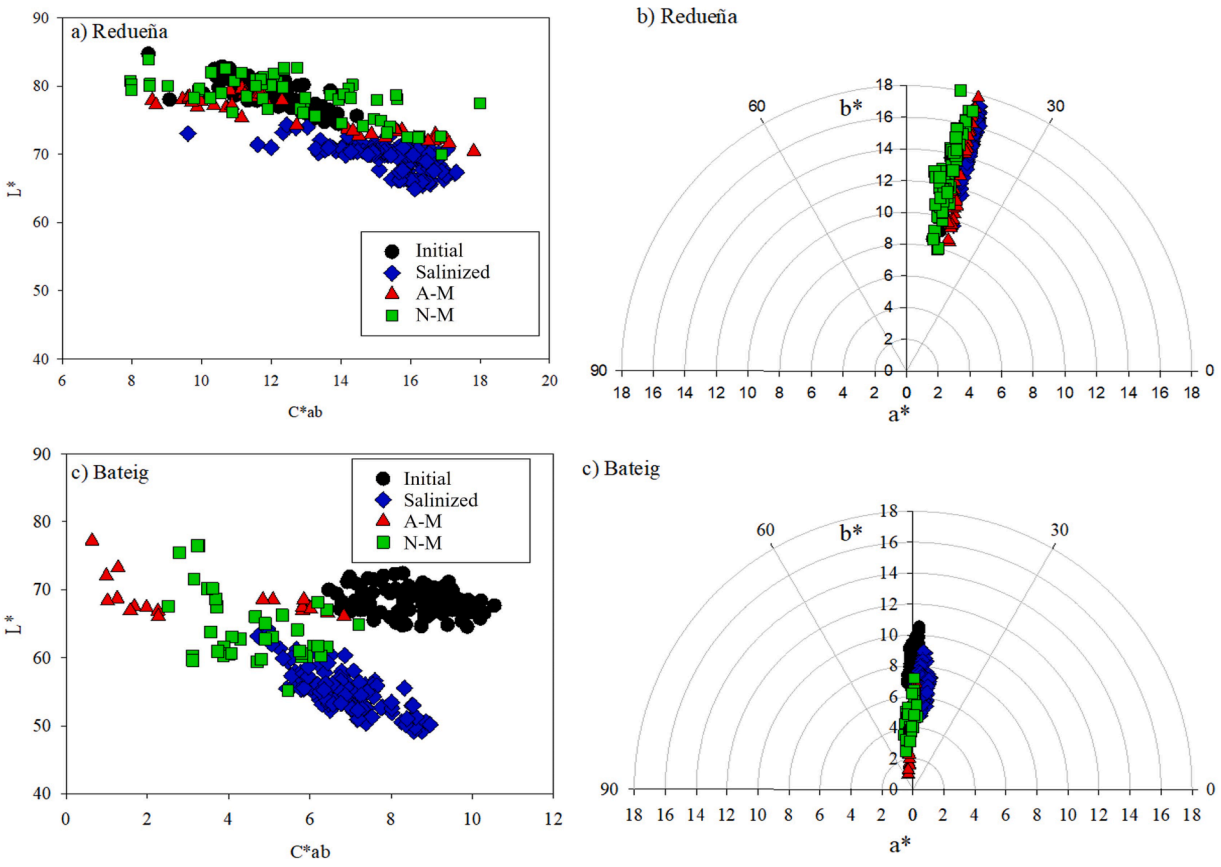


Fig. 12. Scatter plots for L*-C*ab (left) and a*-b* (polar graphs, right) for data collected at different stages of the treatment: initial color; after salt contamination; after treatment with different anion precursors (A-M: ammonium carbonate and N-M: sodium carbonate).

Table 6
Colorimetric differences ΔL*, Δa*, Δb*, and total color difference ΔE*ab at different stages of the treatment: 1: Initial vs After salt contamination; 2: After salt contamination vs After treatment; 3: Initial vs After treatment. Also the risk using the rate proposed by [69] is expressed: 1 (the observer does not notice the difference), 2 (only an experienced observer can notice the difference), 3 (an unexperienced observer also notices the difference), 4 (clear difference in color is noticed), and 5 (observer notices two different colors).

Stone	Precursors		ΔL^*	Δa^*	Δb^*	ΔC^*ab	ΔE^*ab	*Index*
REDUEÑA	**–**	1 vs 2	−9.32	1.56	3.30	3.58	**10.03**	5
	A-M	2 vs 3	5.67	−0.86	−3.08	−3.20	**6.56**	5
		1 vs 3	−3.61	0.78	0.72	0.88	**3.93**	4
	N-M	2 vs 3	8.44	−1.35	−2.19	−2.44	**8.83**	5
		1 vs 3	−0.57	0.06	0.38	0.38	**1.04**	2
BATEIG	**–**	1 vs 2	−12.87	0.54	−1.98	−1.95	**13.04**	5
	A-M	2 vs 3	15.36	−0.80	−3.04	−3.01	**15.68**	5
		1 vs 3	3.48	−0.28	−5.32	−5.27	**6.48**	5
	N-M	2 vs 3	8.38	−0.80	−2.18	−2.20	**8.70**	5
		1 vs 3	−4.65	−0.25	−4.25	−4.25	**6.70**	5

caused by this method is influenced by the original color of the material to be treated. However, although these changes are easily perceptible by the human eye, the treatment cannot be considered as a high-risk intervention since the treatment tends to return the original color of the stones.

4. Conclusions

The main conclusion drawn from this study is that the use of electrokinetic treatments following the proposed procedure allows to.

(1) Completely desalinate stone materials highly contaminated with salts, reaching percentages of effectiveness close to 100 % for all anions, while consolidating the material by the precipitation of inorganic compounds, in this case, calcium magnesium carbonates with different degrees of hydration, in the pores by the continued emptying of salts.

In particular, in both rocks, hydrated phases of carbonates crystallized, some of them metastable, which occupied the pores, reducing the porosity. The increase in the Mg content after A-M and N-M treatments gave rise to Mg-enriched phases in the dolostone and limestone.

The N-M treatment with higher pH led to the dissolution of the dolomite in the dolostone, giving rise to two types of dolomite with different Mg/Ca ratios and calcium enrichment on the surface. Two kinds of Mg-rich calcite with different Mg/Ca ratios also crystallized in the limestone.

(2) From the mineralogical and textural analysis, it was possible to identify specific similarities and differences as a consequence of the treatments due to the inherent textural properties of the original rock. Salt crystallization was different in Redueña dolostone and Bateig limestone due to differences in the pore structure on the deposition surface, which conditioned their adherence and dispersion. In this sense, the limestone pore structure, being more compact and less porous, with tiny pores without evidence of intercrystalline porosity, influenced the deposition of salts, facilitating the formation of a layer of better-defined surface crystals.
(3) The new formation of crystals as a consequence of the desalination and consolidation treatments with different precursors and pH (pH = 9 and pH = 12), managed to eliminate the salts, which initially increased the surface porosity with a notable reduction in the treatment at a higher pH (N-M). This fact shows that the pH of the precursor solutions influences the consolidation efficiency since the yield of this process, regardless of the treated material, was higher when the supplied carbonate came as a carbonate ion rather than as a bicarbonate ion.
(4) The treatment makes it possible to recover part of the original appearance of the rock lost due to the entry of salts.

In short, the treatment has been satisfactory, and its extrapolation to actual surfaces, such as walls and columns, as has already occurred with desalination treatments, is feasible. Only it must consider 1) the potential that will have to be applied from the power supply to allow an adequate current flow to force the proper mobilization of the ions. 2) the distribution of the compartments, which can be placed in direct mode (i.e., facing each other) or in indirect mode (i.e., in parallel on the same surface). 3) The composition of the solutions supplying the precursors will depend on the nature of the selected material to treat.

Funding

This research was funded by the Autonomous Region of Madrid's Top Heritage Programme (S2018/NMT-4372).

CRediT authorship contribution statement

J. Feijoo: Writing – original draft, Visualization, Validation, Supervision, Methodology, Formal analysis, Conceptualization. **L.S. Gomez-Villalba:** Writing – original draft, Visualization, Validation, Methodology, Formal analysis. **R. Fort:** Writing – original draft, Visualization, Supervision, Resources, Funding acquisition, Formal analysis. **M.E. Rabanal:** Investigation, Methodology, Validation.

Declaration of Competing Interest

The authors declare that they have no known competing financial interests or personal relationships that could have appeared to influence the work reported in this paper.

Data availability

Data will be made available on request.

Acknowledgments

Special acknowledgments to the professional support of the Interdisciplinary Thematic Platform from CSIC Open Heritage: Research and Society (PTI-PAIS) and to the Defense University Center at the Spanish Naval Academy (CUD-ENM). Also, thank Mr. Daniel Jordan for his review of the English text.

Appendix A. Supplementary data

Supplementary data to this article can be found online at https://doi.org/10.1016/j.conbuildmat.2023.133686.

References

[1] A.E. Charola, Salts in the Deterioration of Porous Materials: An Overview, J. Am. Inst. Conserv. 39 (2000) 327–343, https://doi.org/10.1179/019713600806113176.
[2] R.M. Espinosa-Marzal, G.W. Scherer, Mechanisms of damage by salt, Geol. Soc. London Spec. Publ. (2010), https://doi.org/10.1144/sp331.5.
[3] G.W. Scherer, Crystallization in pores, Cem. Concr. Res. 29 (1999) 1347–1358, https://doi.org/10.1016/S0008-8846(99)00002-2.
[4] A. La Iglesia, V. González, V. López-Acevedo, C. Viedma, Salt crystallization in porous construction materials I Estimation of crystallization pressure, J. Cryst. Growth 177 (1997) 111–118, https://doi.org/10.1016/S0022-0248(96)01072-X.
[5] M. Sato, T. Hattanji, A laboratory experiment on salt weathering by humidity change: salt damage induced by deliquescence and hydration, Prog Earth Planet Sci (2018), https://doi.org/10.1186/s40645-018-0241-2.
[6] R.M. Espinosa Marzal, G.W. Scherer, Crystallization of sodium sulfate salts in limestone, Environ. Geol. (2008), https://doi.org/10.1007/s00254-008-1441-7.
[7] R.J. Flatt, Salt damage in porous materials: How high supersaturations are generated, J. Cryst. Growth (2002), https://doi.org/10.1016/S0022-0248(02)01429-X.
[8] ICOMOS International Scientific Committee for Stone (ISCS), ICOMOS-ISCS: Illustrated glossary on stone deterioration patterns, 2008. https://doi.org/10.3109/14767058.2010.497569.
[9] B. Menéndez, Estimators of the impact of climate change in salt weathering of cultural heritage, Geosci. (2018), https://doi.org/10.3390/geosciences8110401.
[10] D. Benavente, P. Brimblecombe, Salt weathering and climate change, New Trends Anal. Environ. Cult. Herit. Chem. (2008).
[11] B. Silva, B. Prieto, T. Rivas, L. Pereira, Gypsum-induced decay in granite monuments in Northwestern Spain, Mater. Constr. (2010), https://doi.org/10.3989/mc.2010.46808.
[12] W. Kloppmann, P. Bromblet, J.M. Vallet, V. Vergès-Belmin, O. Rolland, C. Guerrot, C. Gosselin, Building materials as intrinsic sources of sulphate: A hidden face of salt weathering of historical monuments investigated through multi-isotope tracing (B, O, S), Sci. Total Environ. (2011), https://doi.org/10.1016/j.scitotenv.2011.01.008.
[13] P. Lopez-Arce, J. Garcia-Guinea, D. Benavente, L. Tormo, E. Doehne, Deterioration of dolostone by magnesium sulphate salt: An example of incompatible building materials at Bonaval Monastery, Spain, Constr. Build. Mater. (2009), https://doi.org/10.1016/j.conbuildmat.2008.04.001.
[14] N. Schleicher, C.R. Hernández, Source identification of sulphate forming salts on sandstones from monuments in Salamanca, Spain-a stable isotope approach, Environ. Sci. Pollut. Res. (2010), https://doi.org/10.1007/s11356-009-0196-3.
[15] J. Simão, E. Ruiz-Agudo, C. Rodriguez-Navarro, Effects of particulate matter from gasoline and diesel vehicle exhaust emissions on silicate stones sulfation, Atmos. Environ. (2006), https://doi.org/10.1016/j.atmosenv.2006.06.016.
[16] N. Otero, A. Soler, Sulphur isotopes as tracers of the influence of potash mining in groundwater salinisation in the Llobregat Basin (NE Spain), Water Res. (2002), https://doi.org/10.1016/S0043-1354(02)00125-2.
[17] K. Knöller, A. Fauville, B. Mayer, G. Strauch, K. Friese, J. Veizer, Sulfur cycling in an acid mining lake and its vicinity in Lusatia, Germany, Chem. Geol. (2004), https://doi.org/10.1016/j.chemgeo.2003.11.009.
[18] B.A. Lubelli, Sodium chloride damage to porous building materials, TU Delft, Delft Univ. Technol, 2006. PhD Thesis.
[19] B. Silva, T. Rivas, E. García-Rodeja, B. Prieto, Distribution of ions of marine origin in Galicia (NW Spain) as a function of distance from the sea, Atmos. Environ. 41 (2007) 4396–4407, https://doi.org/10.1016/J.ATMOSENV.2007.01.045.
[20] A. Burgos-Cara, E. Ruiz-Agudo, C. Rodriguez-Navarro, Effectiveness of oxalic acid treatments for the protection of marble surfaces, Mater. Des. (2017), https://doi.org/10.1016/j.matdes.2016.11.037.
[21] S. Siegesmund, R. Snethlage, Stone in architecture: Properties, durability, 2011. https://doi.org/10.1007/978-3-642-14475-2.
[22] K. Zoghlami, Las areniscas miocénicas de la formación fortuna utilizadas en la construcción del acueducto romano de Zaghouan-Cartago, 2003 PhD Thesis.
[23] A. Shekofteh, E. Molina, A. Arizzi, G. Cultrone, H. Ahmadi, M. Yazdi, Characterization and damage assessment of stones used in the Pasargadae World Heritage Site, Achaemenian period, Int. J. Archit. Herit. (2019), https://doi.org/10.1080/15583058.2018.1436728.
[24] E.V. Sturm, O. Frank-Kamenetskaya, D. Vlasov, M. Zelenskaya, K. Sazanova, A. Rusakov, R. Kniep, Crystallization of calcium oxalate hydrates by interaction of calcite marble with fungus Aspergillus Niger, Am. Mineral. (2015), https://doi.org/10.2138/am-2015-5104.
[25] M. Gómez-Heras, D. Benavente, M. Álvarez de Buergo, R. Fort, Soluble salt minerals from pigeon droppings as potential contributors to the decay of stone based cultural heritage, Eur. J. Mineral. (2004), https://doi.org/10.1127/0935-1221/2004/0016-0505.
[26] Y. Jiang, Sources of sulfur in the Nandong underground river system, southwest China: A chemical and isotopic reconnaissance, Appl. Geochemistry. (2012), https://doi.org/10.1016/j.apgeochem.2012.05.001.

[27] C.M. Grossi, R.M. Esbert, Las sales solubles en el deterioro de rocas monumentales, Revisión Bibliográfica, Mater. Construcción. (1994), https://doi.org/10.3989/mc.1994.v44.i235.579.
[28] P. López-Arce, R. Fort, M. Gómez-Heras, E. Pérez-Monserrat, M.J. Varas-Muriel, Preservation strategies for avoidance of salt crystallisation in El Paular Monastery cloister, Madrid, Spain, Environ, Earth Sci. 63 (2010) 1487–1509, https://doi.org/10.1007/s12665-010-0733-x.
[29] J. Unruh, A Revised Endpoint for Ceramics Desalination at the Archaeological Site of Gordion, Turkey, Stud. Conserv. (2007), https://doi.org/10.2307/1506839.
[30] N. Husillos-Rodríguez, P.M. Carmona-Quiroga, S. Martínez-Ramírez, M.T. Blanco-Varela, R. Fort, Sacrificial mortars for surface desalination, Constr. Build. Mater. 173 (2018) 452–460, https://doi.org/10.1016/j.conbuildmat.2018.04.029.
[31] M. Auras, J.S.J.S. Albertsen, Poultices and mortars for salt contaminated masonry and stone objects, Salt Weather. Build. Stone Sculpt. (2008) 1–32.
[32] V. Vergès-Belmin, H. Siedel, Desalination of Masonries and Monumental Sculptures by Poulticing: A Review, Restor. Build. Monum. an Int. J. = Bauinstandsetz. Und Baudenkmalpfl. Eine Int. Zeitschrift. (2005), https://doi.org/10.1515/rbm-2005-6000.
[33] J. Feijoo, D. Ergenç, R. Fort, M.Á. de Buergo, Addition of ferrocyanide-based compounds to repairing joint lime mortars as a protective method for porous building materials against sodium chloride damage, Mater. Struct. Constr. 54 (2021), https://doi.org/10.1617/S11527-020-01596-4.
[34] T. Rivas, J. Feijoo, I. de Rosario, J. Taboada, Use of Ferrocyanides on Granite Desalination by Immersion and Poultice-Based Methods, Int. J. Archit. Herit. 11 (2017) 588–606, https://doi.org/10.1080/15583058.2016.1277282.
[35] C. Selwitz, E. Doehne, The evaluation of crystallization modifiers for controlling salt damage to limestone, J. Cult. Herit. 3 (2002) 205–216, https://doi.org/10.1016/S1296-2074(02)01182-2.
[36] D. Ergenç, J. Feijoo, R. Fort, M. Alvarez de Buergo, Effects of potassium ferrocyanide used for desalination on lime composite performances in different curing regimes, Constr. Build. Mater. 259 (2020), 120409, https://doi.org/10.1016/J.CONBUILDMAT.2020.120409.
[37] J. Feijoo, X.R. Nóvoa, T. Rivas, L.M. Ottosen, Enhancing the efficiency of electrochemical desalination of stones: a proton pump approach, Mater. Struct. Constr. 51 (2018), https://doi.org/10.1617/s11527-018-1224-x.
[38] J. Feijoo, T. Rivas, X.R. Nóvoa, L.M. Ottosen, New Double Electrode System for the Electrochemical Desalination of Building Stones, Int. J. Archit. Herit. 00 (2018) 1–16, https://doi.org/10.1080/15583058.2018.1561962.
[39] J. Feijoo, T. Rivas, X.R. Nóvoa, I. de Rosario, J. Otero, In situ desalination of a granitic column by the electrokinetic method, Int. J. Archit. Herit. 12 (2018) 63–74, https://doi.org/10.1080/15583058.2017.1370509.
[40] J. Feijoo, L.M. Ottosen, O. Matyscak, R. Fort, Electrokinetic desalination of a farmhouse applying a proton pump approach. First in situ experience, Constr. Build. Mater. 243 (2020), https://doi.org/10.1016/j.conbuildmat.2020.118308.
[41] J. Correia, F. Matero, Calcium tartrate tetrahydrate preconsolidation of salt-contaminated limestone at mission San José y San Miguel de Aguayo, J. Am. Inst. Conserv. (2008), https://doi.org/10.1179/019713608806112160.
[42] J.W. Lukaszewicz, The influence of pre-consolidation with ethyl silicate on soluble salts removal, in: Proc. 8th Int. Congr. Deterior. Conserv. Stone Berlin, 30. Sept.-4. Oct. 1996, 1996.
[43] J. Feijoo, O. Matyščák, L.M. Ottosen, T. Rivas, X.R. Nóvoa, Electrokinetic desalination of protruded areas of stone avoiding the direct contact with electrodes, Mater. Struct. Constr. 50 (2017), https://doi.org/10.1617/S11527-016-0946-X.
[44] L.M. Ottosen, L.C.H. Andersson, Electrode placement during electro-desalination of NaCl contaminated sandstone – simulating treatment of carved stones, Proc. 4th Int. Conf. Salt Weather. Build. Stone Sculpt. (2017) 150–157.
[45] I. de Rosario, T. Rivas, G. Buceta, J. Feijoo, M.J. Mosquera, Surfactant-Synthesized Consolidants Applied To A Granitic Medieval Necropolis In NW Spain. Laboratory And In Situ Effectiveness Evaluation, Int. J Archit. Herit. 11 (2017) 1166–1176, https://doi.org/10.1080/15583058.2017.1354097.
[46] G.W. Scherer, G.S. Wheeler, Silicate consolidants for stone, Key Eng. Mater. (2009), https://doi.org/10.4028/0-87849-365-4.1.
[47] M. Luna, J.J. Delgado, M.L.A. Gil, M.J. Mosquera, TiO2-SiO2 coatings with a low content of AuNPs for producing self-cleaning building materials, Nanomaterials (2018), https://doi.org/10.3390/nano8030177.
[48] G. Wheeler, Alkoxysilanes and the Consolidation of Stone, 2005. https://doi.org/10.1007/s13398-014-0173-7.2.
[49] J. Feijoo, X.R. Nóvoa, T. Rivas, Electrokinetic treatment to increase bearing capacity and durability of a granite, Mater. Struct. 50 (251) (2017) 1–15, https://doi.org/10.1617/s11527-017-1123-6.
[50] J. Feijoo, L.M. Ottosen, X.R. Nóvoa, T. Rivas, I. de Rosario, An improved electrokinetic method to consolidate porous materials, Mater. Struct. 50 (2017), https://doi.org/10.1617/s11527-017-1063-1.
[51] J. Feijoo, R. Fort, L.S. Gomez-Villalba, M.E. Rabanal, L.M. Ottosen, Electroprecipitation of Magnesium and Calcium Compounds for Weathering Protection of Ornamental Rocks, Cryst. Growth Des. 20 (2020) 2337–2355, https://doi.org/10.1021/acs.cgd.9b01497.
[52] J. Feijoo, L.S. Gomez-Villalba, A. de los Ríos, R. Fort, Electroprecipitation of inorganic borates, with different solubility, within monumental stones to avoid fungal colonization, Constructionand Building Materials 368 (2023), 130435, https://doi.org/10.1016/j.conbuildmat.2023.130435.
[53] B. Sena da Fonseca, A.P. Ferreira Pinto, M. Rucha, M.M. Alves, M.F. Montemor, Damaging effects of salt crystallization on a porous limestone after consolidation treatments, Constr. Build. Mater. 374 (2023), 130967, https://doi.org/10.1016/j.conbuildmat.2023.130967.
[54] M. Matteini, Inorganic treatments for the consolidation and protection of stone artefacts, Conserv. Sci. Cult. Herit. 8 (2008) 13–27.
[55] R. Fort, B. Fernández-Revuelta, M.J. Varas, M. Álvarez De Buergo, M. Taborda-Duarte, Influence of anisotropy on the durability of Madrid-region Cretaceous dolostone exposed to salt crystallization processes, Mater. Constr. (2008), https://doi.org/10.3989/mc.2008.v58.i289-290.74.
[56] R. Fort, A. Bernabéu, M.A. García Del Cura, M.C. López De Azcona, S. Ordóñez, F. Mingarro, Novelda Stone: Widely used within the spanish architectural heritage, Mater. Constr. (2002).
[57] A. Arnold, K. Zehnder, Salt weathering on monuments, La Conserv. Dei Monum. Nel Bacino Del Mediterr. Influ. Dell'ambiente Costiero e Dello Spray Mar. Sulla Pietra Calcarea e Sul Marmo Atti Del 1o Simp. Internazionale, Bari 7-10 Giugno, 1989 = Conserv. Monum. Mediter. (1990).
[58] P.W. Atkins, Physical Chemistry, 6th editio, Oxford University Press, Oxford., 1998.
[59] UNE-EN 1936:2007, Natural stone test methods - Determination of real density and apparent density, and of total and open porosity, (n.d.).
[60] UNE-EN 1925:1999, Natural stone test methods - Determination of water absorption coefficient by capillarity, (n.d.).
[61] A. Bernabeu, E. Expósito, V. Montiel, S. Ordóñez, A. Aldaz, A new electrochemical method for consolidation of porous rocks, Electrochem. Commun. 3 (2001) 122–127, https://doi.org/10.1016/S1388-2481(01)00117-5.
[62] M. Gomez-Heras, D. Benavente, C. Pla, J. Martinez-Martinez, R. Fort, V. Brotons, Ultrasonic pulse velocity as a way of improving uniaxial compressive strength estimations from Leeb hardness measurements, Constr. Build. Mater. 261 (2020), 119996, https://doi.org/10.1016/j.conbuildmat.2020.119996.
[63] T. Lee, J. Lee, H. Choi, Assessment of Strength Development at Hardened Stage on High-Strength Concrete Using NDT, Appl. Sci. 10 (2020), https://doi.org/10.3390/app10186261.
[64] J.-S. Kim, Y.-S. Shin, K.-O. Kim, A Study on the proposal of Strength Presumption Equation of Concrete Using Admixture by Nondestructive Testing, J. Korean Inst. Build. Constr. 6 (2006) 59–66, https://doi.org/10.5345/jkic.2006.6.3.059.
[65] E. Vasanelli, D. Colangiuli, A. Calia, M. Sileo, M.A. Aiello, Ultrasonic pulse velocity for the evaluation of physical and mechanical properties of a highly porous building limestone, Ultrasonics 60 (2015) 33–40, https://doi.org/10.1016/j.ultras.2015.02.010.
[66] J. Feijoo, X.R. Nóvoa, T. Rivas, M.J. Mosquera, J. Taboada, C. Montojo, F. Carrera, Granite desalination using electromigration. Influence of type of granite and saline contaminant, J. Cult. Herit. 14 (2013) 365–376, https://doi.org/10.1016/J.CULHER.2012.09.004.
[67] J. Feijoo, L.M. Ottosen, J.S. Pozo-Antonio, Influence of the properties of granite and sandstone in the desalination process by electrokinetic technique, Electrochim. Acta 181 (2015) 280–287, https://doi.org/10.1016/J.ELECTACTA.2015.06.006.
[68] B. Lubelli, R.P.J. van Hees, Desalination of masonry structures: Fine tuning of pore size distribution of poultices to substrate properties, J. Cult. Herit. 11 (2010) 10–18, https://doi.org/10.1016/j.culher.2009.03.005.
[69] W.S. Mokrzycki, M. Tatol, Color difference Delta E - A survey, Mach. Graph, Vis, 2011.
[70] Á. La Iglesia, M.A. García del Cura, S. Ordóñez, A. Bernabeu, Estudio de los filosilicatos de la «Piedra Bateig» (Neógeno de la provincia de Alicante), accessed October 14, 2022, Geogaceta 23 (1998) 79–82, http://hdl.handle.net/10272/10431.
[71] D.F. Sibley, The origin of common dolomite fabrics; clues from the Pliocene, J. Sediment. Res. 52 (1982) 1087–1110, https://doi.org/10.1306/212F80DF-2B24-11D7-8648000102C1865D.
[72] R.E. Woody, J.M. Gregg, L.F. Koederitz, Effect of texture on petrophysical properties of dolomite: Evidence from the Cambrian-Ordovician of southeastern Missouri, American Association of Petroleum Geologists Bulletin 80 (1996) 119–132, https://doi.org/10.1306/64ed8764-1724-11d7-8645000102c1865d.
[73] ÖNOR.M.B. 3355-1 Trockenlegung von feuchtemMauerwerk — Teil 1: Bauwerksdiagnose und Planungsgrundlagen Berlin. ASI Austrian Standards Institute ÖsterreichischesNormungsinstitut (Herausgeber) Deutschland, Bundesrepublik, BeuthVerlag, 1 (2006) 3355.
[74] Y.B. Acar, A.N. Alshawabkeh, Principles of Electrokinetic Remediation, Environ. Sci. Tech. (1993), https://doi.org/10.1021/es00049a002.
[75] L.K. Yakhontova, Sergeevite, a new hydrous carbonate of magnesium and calcium, Int. Geol. Rev. 24 (1982) 105–110.
[76] J.W. Singer, Formation and Transformation of Amorphous Calcium-Magnesium Carbonates in Synthetic Seawater, Alfred University, 2013.
[77] G. Schimmel, Basische Calciumcarbonate, Naturwissenschaften 57 (1970) 38–39, https://doi.org/10.1007/BF00593556.
[78] Y. Sheng Han, G. Hadiko, M. Fuji, M. Takahashi, Crystallization and transformation of vaterite at controlled pH, J. Cryst. Growth 289 (2006) 269–274, https://doi.org/10.1016/j.jcrysgro.2005.11.011.
[79] W. Kim, K. Jeong, H. Choi, T. Lee, Correlation Analysis of Ultrasonic Pulse Velocity and, (2022).
[80] L.S. Gomez-Villalba, J. Feijoo, M.E. Rabanal, R. Fort, In-situ electrochemical synthesis of inorganic compounds for materials conservation: Assessment of their effects on the porous structure, Ceram. Int. 47 (2021) 30406–30424, https://doi.org/10.1016/j.ceramint.2021.07.221.